Spatial distribution of aerosol microphysical and optical properties and direct radiative effect from the China Aerosol Remote Sensing Network

Huizheng Che[1*], Xiangao Xia[2,3], Hujia Zhao[1,4], Oleg Dubovik[5], Brent N. Holben[6], Philippe Goloub[5], Emilio Cuevas-Agulló[7], Victor Estelles[8], Yaqiang Wang[1], Jun Zhu[9] Bing Qi[10], Wei Gong [11], Honglong Yang[12], Renjian Zhang[13], Leiku Yang[14], Jing Chen[15], Hong Wang[1], Yu Zheng[1], Ke Gui[1,2],Xiaochun Zhang[16], Xiaoye Zhang[1*]

1 State Key Laboratory of Severe Weather (LASW) and Key Laboratory of Atmospheric Chemistry (LAC), Chinese Academy of Meteorological Sciences, CMA, Beijing, 100081, China

2 Laboratory for Middle Atmosphere and Global Environment Observation (LAGEO), Institute of Atmospheric Physics, Chinese Academy of Sciences, Beijing, 100029, China

3 University of Chinese Academy of Science, Beijing, 100049, China

4 Institute of Atmospheric Environment, CMA, Shenyang, 110016, China

5 Laboratoire d'Optique Amosphérique, Université des Sciences et Technologies de Lille, 59655, Villeneuve d'Ascq, France

6 NASA Goddard Space Flight Center, Greenbelt, MD, USA

7 Centro de Investigación Atmosférica de Izaña, AEMET, 38001 Santa Cruz de Tenerife , Spain

8 Dept. Fisica de la Terra i Termodinamica, Universitat de Valencia, C/ Dr. Moliner 50, 46100 Burjassot, Spain

9 Collaborative Innovation Center on Forecast and Evaluation of Meteorological Disasters, Nanjing University of Information Science & Technology, Nanjing, 210044, China

10 Hangzhou Meteorological Bureau, Hangzhou, 310051, China

11 State Key Laboratory of Information Engineering in Surveying, Mapping and Remote Sensing, Wuhan University, Wuhan, 430079, China

12 Shenzhen Meteorological Bureau, Shenzhen, 518040, China

13 Key Laboratory of Regional Climate-Environment Research for Temperate East Asia, Institute of Atmospheric Physics, Beijing, 100029, Chinese Academy of Sciences.

14 School of Surveying and Land Information Engineering, Henan Polytechnic University, Jiaozuo, 454000, China

15 Shijiazhuang Meteorological Bureau, Shijiazhuang, 050081, China

16 Meteorological Observation Center, CMA, Beijing, 100081

Corresponding author: chehz@cma.gov.cn & xiaoye@cma.gov.cn

Abstract

Multi-year observations of aerosol microphysical and optical properties obtained through ground-based remote sensing at 50 China Aerosol Remote Sensing Network (CARSNET) sites were used to characterize the aerosol climatology for representative remote, rural, and urban areas over China to assess effects on climate. The annual mean effective radii for total particles (R_{efft}) decreased from north to south and from rural to urban sites, and high total particle volumes were found at the urban sites. The aerosol optical depth at 440 nm (AOD_{440nm}) increased from remote/rural sites (0.12) to urban sites (0.79), and the extinction Ångström exponent ($EAE_{440\text{-}870nm}$) increased from 0.71 at the arid/semi-arid sites to 1.15 at the urban sites, presumably due to anthropogenic emissions. Single scattering albedos ($SSA_{440\ nm}$) ranged from 0.88 to 0.92 indicating slightly to strongly absorbing aerosols. Absorption AOD_{440nm}'s were 0.01 at the remote sites versus 0.07 at the urban sites. The average direct aerosol radiative effect (DARE) at the bottom of atmosphere increased from the sites in the remote (-24.40 W/m^2) to the urban area (-103.28 W/m^2) indicating increased cooling at the latter. The DARE for the top of the atmosphere increased from -4.79 W/m^2 at the remote sites to -30.05 W/m^2 at the urban sites, indicating overall cooling effects for the earth-atmosphere system. A classification method based on $SSA_{440\ nm}$, fine mode fraction (FMF), and $EAE_{440\text{-}870\ nm}$ showed that coarse mode particles (mainly dust) were dominant at the rural sites near the northwestern deserts, while light-absorbing, fine-mode particles were important at most urban sites. This study will be important for understanding aerosol climate effects and regional environmental pollution, and the results will provide useful information for satellite validation and the improvement of climate modelings.

Keywords: aerosol optical properties; direct aerosol radiative effect; aerosol type; climatology; China Aerosol Remote Sensing Network

1. Introduction

Atmospheric aerosols have important direct effects on climate because they can scatter and absorb radiant energy and in so doing affect the Earth's energy balance (Charlson et al., 1992; Yang et al., 2016). Meanwhile, the aerosols can be served as cloud condensation nuclei or ice nuclei to affect the climate indirectly through aerosol–cloud interactions (Twomey et al., 1984; Garrett et al., 2006; Zhao et al., 2015; Xie et al., 2013). The optical properties of the aerosol determine the particles' direct effects on the Earth's radiative balance and weather-climate change (Ramanathan et al., 2001; Eck et al., 2005; Myhre, 2009; Zhao et al., 2018). Aerosol optical depth (AOD) is one of the key measures of the total aerosol extinction effects on climate (Breon et al., 2002), and the extinction Ångström exponent (EAE) with spectral dependence can be used to obtain the information about aerosol size distributions (Gobbi et al., 2007; Eck et al., 1999; Zheng et al., 2017). The aerosols' absorptivity depends on particle composition is a key determinant to calculate the direct aerosol radiative effect (Haywood and Shine, 1995; Li et al., 2016; Zheng et al., 2018), and the single scattering albedo (SSA) is the parameter has spectral dependence to distinguish major aerosol particle types (Jacobson et al., 2000; Dubovik et al., 2002; Gelencser et al., 2004; Russell et al., 2010; Giles et al., 2012).

With the recognition of the importance for climate, the aerosol optical properties have been obtained from ground-based monitoring networks worldwide; some of the major networks include AERONET-Aerosol Robotic Network) (Holben et al., 1998) and its sub-networks of PHOTONS-PHOtométrie pour le Traitement Opérationnel de Normalisation Satellitaire, AEROCAN-Canadian Sun-Photometer Network, and RIMA-Iberian Network for aerosol measurements ((Goloub et al., 2007; Bokoye et al., 2001; Prats et al., 2011), SKYNET-SKYrad Network (Takamura and Nakajima, 2004; Che et al., 2008), EARLINET-European aerosol Lidar network (Pappalardo et al., 2014), the GAW-PFR Network-Global Atmosphere Watch

Programmer-Precision Filter Radiometers (Wehrli, 2002; Estellés et al., 2012),. The CARSNET-China Aerosol Remote Sensing NETwork, the CSHNET-Chinese Sun Hazemeter Network and the SONET-Sun–Sky Radiometer Observation Network have been established to measure aerosol optical properties in China (Che et al., 2009a, 2015; Xin et al., 2007; Li et al., 2018). Furthermore, the aerosol optical properties have also been used in comprehensive studies of aerosol physical characteristics and chemical composition in many regions of China (Che et al., 2009c, 2018; Zhao et al., 2018).

China has become one of the largest aerosol sources in the world associated with its rapid economic development, and this has caused significant effects on local environments and regional climate (Che et al., 2005; Xia, 2010; Li et al., 2016; Yang et al., 2018, 2019; Zhao et al., 2019). There have been numerous studies that have focused on aerosol optical properties obtained though ground-based remote sensing methods in China (Luo et al., 2002; Li et al., 2003; Duan and Mao, 2007). A few researches have paid more attention to the aerosol optical properties and its radiative effects over the urban-industrial areas as well as at coastal sites in northeastern and eastern China (Wang et al., 2010; Xin et al., 2011; Xia et al., 2007; Zhao et al., 2016; Wu et al. 2012; Shen et al., 2019). Many studies of aerosol optical properties were conducted in northern China with high aerosol loadings, such as the Beijing-Tianjin-Hebei region (Che et al. 2014; Xia et al., 2013; Fan et al., 2006; Xie et al., 2008; Zhang et al., 2019; Yang et al., 2019; Zhao et al., 2018). Aerosol optical properties also have been investigated at Hefei, Shouxian, Nanjing, Taihu, Shanghai and other sites in eastern China (Lee et al., 2010; He et al., 2012; Zhuang et al., 2014; Wang Z et al., 2015; Che et al., 2018). Some studies of aerosol optical properties have been made in southern China (Wang et al., 2015; Tao et al., 2014), and those at remote and rural sites in China provide information on regional background conditions (Che et al., 2009b; Wang et al., 2010; Xue et al., 2011; Zhu et al., 2014; Yuan et al., 2014).

China's vast size, varied terrain, and heterogeneity of aerosol sources, has led to strong temporal and spatial variability in aerosol optical and physical properties. The mixtures of aerosol types at most sites are complex, and aerosol populations' size and composition are affected by their sources, transformations that occurring during transportation and removing processes (Cao et al., 2007; Wang et al., 2007; Zhang et al., 2013; Wan et al., 2015). National scale, ground-based measurements of aerosol microphysical and its optical properties obtained from the sunphotometer provide for a better understanding of the aerosols' climate effects over the different regions of China. The measurements of greatest interest include aerosol size distributions (volume and aerosol effective radii), optical properties (AOD, AE, SSA, absorption AOD) because those data can at least be used to evaluate direct radiative effect.

The aim of this study was focused on the investigation of the climatological spatial distribution of aerosol microphysical and optical properties over regional-scales using spatial distribution data from the national CARSNET network. The data were collected at CARSNET sites, which include sites in the remote, rural and urban area, with the same calibration procedures and calculation algorithms were used at all sites. As a result, the data are directly comparable among sites (Che et al., 2009a), and the results can be provided to characterize the regional distribution and temporal variation of aerosol optical properties. This research focused on aerosol climate effects and regional environmental pollution, and the results should be useful for satellite validations and for the improvement of models in the future. The remainder of this paper is organized as following: Section 2 firstly describes the sites in detail, and then introduced the methods in data processing of the aerosol optical properties as well as the direct aerosol radiative effect calculation through the retrieved aerosol optical parameters. Section 3 illustrates the aerosol microphysical and optical properties, as well as its direct aerosol radiative effect. An aerosol type classification method is proposed

according to the aerosol optical parameters. Section 4 presents the conclusions of the study.

2 Site description, instruments, and data

2.1 Site description

Sunphotometers (CE-318, Cimel Electronique, Paris, France, see Appendix A,) were installed at 50 CARSNET sites (Fig. 1) from 2010 to 2017. The stations were classified as remote, rural, or urban sites based on administrative division (Appendix Table 1). Three of the remote stations were about more than 3000 m above the sea level on the Tibetan Plateau far from the anthropogenic influences, and one of them was a northwestern regional background site in China. The 23 rural sites represent (a) five sites of desert regions affected by most of dust aerosols rather than anthropogenic particles, (b) two sites affected by both dust and anthropogenic activities on the Loess Plateau, and (c) 16 sites located near or surrounding the large cities relatively strong to the impacts of anthropogenic activities in the central and eastern China. The last category is 24 urban sites located in provincial capitals or heavily populated cities.

2.2 Instruments and calibration

The CE-318 sunphotometers used in this study were calibrated annually, using the CARSNET calibration protocol, to verify the accuracy and reliability of the sky irradiance measurements (Holben et al., 1998; Che et al., 2009; Tao et al., 2014). The reference instruments for CARSNET were periodically calibrated at Izaña, Tenerife, Spain located at 28.31 °N, 16.50 °W (2391.0 m a.s.l.) in conjunction with the AERONET program. There are several different types of the Cimel instruments that have been used at the 50 sites in this network as follows: (1) logical type CE-318 sunphotometers (440 nm, 675 nm, 870 nm, 940 nm, 1020 nm and three 870 nm at the polarization band), (2) numerical type CE-318 sunphotometers (440 nm, 675 nm, 870 nm, 940 nm, 1020 nm and three polarization bands at 870 nm), (3) numerical type CE-318 sunphotometers at eight wavelengths (340 nm, 380 nm, 440 nm, 500 nm, 675

nm, 870 nm, 940 nm, and 1020 nm), (4) and numerical type CE-318 sunphotometers at nine wavelengths (340 nm, 380 nm, 440 nm, 500 nm, 675 nm, 870 nm, 940 nm, 1020 nm and 1640 nm).

Measurements used to retrieve AODs were at 340 nm, 380 nm, 440 nm, 500 nm, 675 nm, 870 nm, 1020 nm, and 1640 nm, while the total precipitable water content was obtained by using those measurements at 940 nm (Holben et al., 1998; Dubovik and King, 2000). The cloud-screened AOD data were calculated by using the ASTPwin software, and extinction Ångström exponents (EAE) were calculated from the instantaneous AODs for wavelengths of 440 nm and 870 nm (Che et al., 2009, 2015). Sites with more than three daily AOD observations and more than 10 monthly AOD observation days were used to calculate the daily and monthly mean AODs and extinction Ångström exponents. The FMF is described as the fraction of fine mode particles of total AOD_{440nm} ($AOD_{fine440\ nm}/AOD_{440\ nm}$).

2.3. Data processing

The aerosol microphysical and optical properties, including volume size distributions (dV(r)/dln(r), the total, fine, and coarse mode aerosol effective radii (R_{effT}, R_{effF}, and R_{effC}, respectively) single-scattering albedo (SSA), complex refractive indices, absorption AODs (AAODs), and absorption Ångström exponents (AAEs), were retrieved from the observational data from the sky scattering channel of the sunphotometers at 440 nm, 670 nm, 870 nm, 1020 nm using the algorithms of Dubovik et al. (2002, 2006). In the process of retrieval, the data of surface albedo (SA) was interpolated or extrapolated to 440 nm, 670 nm, 870 nm, and 1020 nm based on the daily MCD43C3 data, a product from the MODIS-Moderate Resolution Imaging Spectroradiometer surface reflectance (https://ladsweb.modaps.eosdis.nasa.gov/). The algorithm used to calculate aerosol volume size distributions ($dV/\ln r$) was under the assumption of a homogeneous distribution of non-spherical particles following the approach of Dubovik (2006). The sphericity fraction retrieved from the

inversions is defined as: spherical particles/(spheroidal particles + spherical particles) (Giles et al., 2011).

As Dubovik et al. (2002, 2006) defined that all the particles with effective radii < 0.992 μm were considered as fine mode particles; and those > 0.992 μm were considered as coarse mode particles. For the total (R_{effT}), fine (R_{effF}) and coarse (R_{effC}) mode aerosols, the effective radii are calculated by the equation as follows:

$$\mathrm{R_{eff}} = \frac{\int_{\mathrm{r_{min}}}^{\mathrm{r_{max}}} \mathrm{r^3} \frac{\mathrm{dN(r)}}{\mathrm{dlnr}} \mathrm{dlnr}}{\int_{\mathrm{r_{min}}}^{\mathrm{r_{max}}} \mathrm{r^2} \frac{\mathrm{dN(r)}}{\mathrm{dlnr}} \mathrm{dlnr}} \quad (1)$$

Where r_{min} denotes 0.05, 0.05, 0.992 μm and r_{max} denotes 15, 0.992, 15 μm of the total, fine and coarse mode particles, respectively.

The coarse (PV_C) and fine aerosol particle volumes distributions (PV_F) are calculated according to a bimodal lognormal function descript by Whitby (1978), Shettle and Fenn (1979) and Remer and Kaufman (1998):

$$\frac{dV(\mathrm{r})}{d\mathrm{lnr}} = \sum_{i=1}^{2} \frac{\mathrm{C_{v,}}_i}{\sqrt{2\pi}\sigma_i} exp\left[-\frac{\left(lnr - lnr_{V,i}\right)^2}{2\sigma_i^2}\right] \quad (2)$$

where $\mathrm{C_{v,}}_i$ means for the volume concentration; $r_{V,i}$ means the median radius, and σ_i means the standard deviation.

The volume median radius is computed by fine and coarse modes particles as follows:

$$\mathrm{ln}r_{\mathrm{V}} = \frac{\int_{\mathrm{r_{min}}}^{\mathrm{r_{max}}} \mathrm{ln}r \frac{\mathrm{dV(r)}}{\mathrm{dlnr}} \mathrm{dlnr}}{\int_{\mathrm{r_{min}}}^{\mathrm{r_{max}}} \frac{\mathrm{dV(r)}}{\mathrm{dlnr}} \mathrm{dlnr}} \quad (3)$$

Then the standard deviation is calculated from the volume median radius:

$$\sigma_V = \sqrt{\frac{\int_{r_{min}}^{r_{max}} (lnr - lnr_V)^2 \frac{dV(r)}{d\ lnr} d\ lnr}{\int_{r_{min}}^{r_{max}} \frac{dV(r)}{d\ lnr} d\ lnr}} \quad (4)$$

The volume concentration ($\mu m^3/\mu m^2$) is speculated by the following equation:

$$C_V = \int_{r_{min}}^{r_{max}} \frac{dV(r)}{d\ lnr} d\ lnr \quad (5)$$

The SSA was retrieved only for AOD_{440nm} > 0.40; this was done to avoid the larger uncertainty inherent in the lower AOD retrieval according to Dubovik et al. (2002, 2006). The AAOD and AAE for wavelength λ were calculated as follows:

$$\mathrm{AAOD}(\lambda) = [1 - \mathrm{SSA}(\lambda)] \times \mathrm{AOD}(\lambda) \quad (6)$$

$$\mathrm{AAE} = \frac{-\mathrm{dln}[\mathrm{AAOD}(\lambda)]}{\mathrm{dln}(\lambda)} \quad (7)$$

The total AODs' uncertainty was 0.01 to 0.02 according to Eck et al. (1999). The accuracy of SSA retrieved from AOD_{440nm} > 0.50 with solar zenith angles > 50 was 0.03 (Dubovik et al., 2002). The accuracy of the particle volume size distribution was 15–25% between 0.1 μm ≤ r ≤ 7.0 μm and 25–100% in conditions of r < 0.1 μm and r >7μm.

Direct aerosol radiative effect (DARE in W/m^2) was calculated by the radiative transfer module under cloud-free conditions, which is similar to the inversion of AERONET (García et al., 2008; 2012). The DARE at the bottom of the atmosphere (BOA) and the top of the atmosphere (TOA) was defined as the difference in the shortwave radiative fluxes with and without aerosol effects as follows:

$$\mathrm{DARE}_{TOA} = F_{TOA}^{\uparrow 0} - F_{TOA}^{\uparrow} \quad (8)$$

$$\mathrm{DARE}_{BOA} = F_{BOA}^{\downarrow} - F_{BOA}^{\downarrow 0} \quad (9)$$

Where F and F^0 denoted the broadband fluxes including and excluding

aerosols, respectively at the BOA and TOA. The " ↑ " and " ↓ "mean the upward fluxes and downward fluxes, respectively.

In the radiative transfer module, the absorption and multiple scattering effects are taken into account during flux calculations by the Discrete Ordinates (DISORT) approach (Nakajima and Tanaka, 1988; Stamnes et al., 1988). The gaseous distributions and single fixed aerosol vertical distribution (exponential to 1 km) from the multi-layered US standard 1976 atmosphere were used in the radiative flux calculations (García et al., 2008). García et al. (2008) pointed out that the error for the observed solar radiation at the surface in global was +2.1 ± 3.0% for an overestimation of about +9 ± 12 Wm^{-2}. The data used in preparing the figures for the present paper have been made available as an Appendix.

3. Results and discussion

3.1 Spatial distribution of aerosol microphysical properties

A map showing the 50 CARSNET sampling sites and plots of the aerosol volume size distributions (dV/dlnr) at each of the sites is shown in Fig. 1. Generally, the annual mean effective radius of total particles (R_{effT}) decreased from the inland northwest to the southeastern coastal areas. Furthermore, the volume concentration of total particles was found substantially higher at the urban sites. The volume of the coarse mode particles was considerably larger than that of the fine mode particles at the remotes, arid/semi-arid sites and at those sites on the CLP-Chinese Loess Plateau or nearby, indicating that those areas were most strongly affected by larger particles, most likely mineral dust as discussed below.

The average (arithmetic mean) R_{effT} at the remote sites was about 0.47 μm with the volume about 0.05 $\mu m^3/\mu m^2$ (Table 1). A large R_{effT} (0.64 μm) was found at Lhasa, and the total aerosol volume there was 0.05 $\mu m^3/\mu m^2$. These results are consistent with those reports by Li et al. (2018) who found high levels of coarse mode particles at Lhasa due to the presence of mineral dust.

The two other remote sites, Akedala and Shangri-La, had smaller average R_{effT} values than Lhasa (0.36 and 0.39 μm, respectively), and corresponding volumes were 0.06 and 0.03 $\mu m^3/\mu m^2$. The average fine-mode effective radius (R_{effF}) was 0.14 μm at the remote sites, and fine-mode particle fractional volume (PV_F) was 0.01 $\mu m^3/\mu m^2$, while the average coarse-mode effective radii (R_{effC}) was 2.35 μm and the coarse-mode fractional volume (PV_C) was 0.03 $\mu m^3/\mu m^2$. These findings indicated that the contribution of coarse-mode particles to the total volume of aerosol was larger at the remote sites. A study by Cong et al. (2009) at the remote Nam Co site on the Tibetan Plateau showed that dust particles mainly affected the site in spring, while anthropogenic aerosols were prevalent in the summer.

The average R_{effT} at the arid and semi-arid sites (0.55 μm) was larger than at the remote sites, and the total volume of aerosols at the arid/semi-arid sites also was large (0.14 $\mu m^3/\mu m^2$), nearly three times that at the remote sites. Large R_{effT} values (0.71 μm) were found at Tazhong, which is near the northwestern deserts, and the aerosol volume there also was high to 0.30 $\mu m^3/\mu m^2$. Large PV_C's were found at the arid/semi-arid sites (0.05–0.27 $\mu m^3/\mu m^2$). The arithmetic mean R_{effT} (0.49 μm) at the rural sites on or near the CLP had total aerosol volumes (0.15 $\mu m^3/\mu m^2$) similar to those at the arid/semi-arid sites. These results also show a major contribution to the aerosol volumes by coarse-mode particles at the sites in or near the mineral dust source regions. Bi et al. (2011) similarly found that coarse particles dominated the volume-size distribution at the Semi-Arid Climate and Environment Observatory of Lanzhou University (SACOL) on the CLP.

Small R_{effT} values (0.33 μm) were found at the rural sites in eastern China, and relatively high aerosol volumes were observed there (0.18 $\mu m^3/\mu m^2$). In the Yangtze River Delta (YRD) region, the R_{effF} was large range for 0.16–0.17 μm, and the PV_F's were 0.12–0.13 $\mu m^3/\mu m^2$. At the Mt. Longfeng background site in northeastern China, the total particle volume was low (0.08 $\mu m^3/\mu m^2$), which is consistent with minimal anthropogenic influences and low aerosol

loadings. Compared with the other sites, the urban areas had relatively low coarse mode aerosol concentrations, but small particles were plentiful—the average R_{effT} was 0.37 μm and total volume was high at 0.21 $\mu m^3/\mu m^2$. The average R_{effF} of fine-mode particles at the urban sites was 0.16 μm with a PV_F of 0.10 $\mu m^3/\mu m^2$ while the R_{effC} was 2.22 μm and PV_C was 0.11 $\mu m^3/\mu m^2$.

The effective radii and PV_F values showed strong relationships with population density and vehicle emissions at the urban sites. High volumes of fine mode particles occurred at the northeastern urban site of Shenyang (R_{effT} = 0.16 μm, PV_F = 0.12 $\mu m^3/\mu m^2$); at major cities in northern China, including Shijiazhuang (R_{effT} = 0.16 μm, PV_F = 0.12 $\mu m^3/\mu m^2$) and Zhengzhou (R_{effT} = 0.18 μm, PV_F = 0.12 $\mu m^3/\mu m^2$); at Chengdu, a city in the Sichuan Basin of (R_{effT} = 0.21 μm, PV_F = 0.16 $\mu m^3/\mu m^2$); and at the urban regions of Nanning (R_{effT} = 0.18 μm, PV_F = 0.13 $\mu m^3/\mu m^2$) and Panyu (R_{effT} = 0.16 μm, PV_F = 0.10 $\mu m^3/\mu m^2$) in southern China. Overall, these results show that the volumes of fine-mode particles increased at the urban sites where anthropogenic influences were most apparent.

Cheng et al. (2015) found different aerosol volume size distributions for dust and sea salt at Shanghai in the eastern China, and they showed that their relative abundances varied with season and in response to local or long-range transport. Zhao et al. (2018) also reported the effect of sea salt aerosol on the aerosol absorption and radiative effects in the coastal region over northeastern China. Especially the particles hygroscopic growth with different composition observed in special climatic conditions could affect aerosol microphysical properties by geographically variable effects (Zhang et al., 2015; Sun et al., 2010). Like in the YRD region, hygroscopic growth of fine-mode particles could lead to larger AOD and scattering enhancing reported by Sun et al. (2018) and Che et al. (2018). Xia et al. (2019) observed the aerosol hygroscopic growth on fine particle scattering coefficient in Beijing.

3.2 Spatial distributions of AOD and EAE

353 The spatial distributions of $AOD_{440\ nm}$ and $EAE_{440\text{-}870\ nm}$ are shown in Fig. 2.
354 The AOD_{440nm} increased from the remote/rural sites to the urban sites, and as
355 one might expect, the remote sites were the least affected by particle
356 emissions and had the lowest aerosol loadings. For example, the AOD_{440nm} at
357 the remote stations was low and had an average value of 0.12. The Lhasa and
358 Shangri-La sites on the Tibetan Plateau had similar average AOD_{440nm} values
359 of 0.10. These phenomenons are similar to the study of Li et al. (2018), who
360 showed clean air conditions at Lhasa with AOD < 0.1. Cong et al. (2007, 2009)
361 also found a low AOD (0.05) at Nam Co, which was comparable to the
362 background levels at other remote sites.
363 The AOD_{440nm}'s at the arid/semi-arid sites and those on or near the Loess
364 Plateau ranged from 0.32–0.42, which is higher than at the remote sites. The
365 high AOD_{440nm} at Tazhong (0.60), which is near the deserts in northwestern
366 China was likely due to the large aerosol volume of 0.30 $\mu m^3/\mu m^2$ (section 3.1)
367 caused by mineral dust. Indeed, arid and semi-arid regions in northwestern
368 China are important sources of aeolian dust on a global scale (Bi et al., 2011).
369 Li et al. (2012) showed that the contribution of dust to the average AOD at
370 SACOL near Lanzhou was 28.4%. Other sites that showed large AOD_{440nm}
371 include regions with strong anthropogenic influences, such as Dengfeng (0.79)
372 on the North China Plain, Huimin (0.83) in the YRD (0.83 to 0.87) and Huainan
373 (0.91) in the Guanzhong Plain.
374 Compared with the sites just discussed, lower AOD_{440nm}'s were found at
375 the Mt. Longfeng background station of the Northeast China Plain (0.34), the
376 semi-arid rural site as Tongyu in northeastern China (0.23), and the clean
377 Xiyong site in southern China (0.41). Zhu et al. (2014) found a low AOD of 0.28
378 at the North China Plain regional background site. Che et al. (2009c) have
379 pointed out that the large AOD at Lin'an was likely affected by the high aerosol
380 loadings in YRD Region. Among the urban sites in China, large $AOD4_{40nm}$'s
381 were found in the cities with strong influences of anthropogenic activities, such
382 as the Northeastern Plain (Shenyang 0.89), North China Plain (Zhengzhou

0.99), Central China (Wuhan 1.00) and Sichuan Basin (Chengdu 1.17); the average value for these sites was 0.79. Lower AOD_{440nm}'s, that is < 0.50, occurred at remote sites in northwestern China, including Urumqi (0.42), Yinchuan (0.37); those sites are affected less by industrial activities and the population densities are lower compared with the sites in northern or eastern China.

It is worth noting that the particle emissions in or around the urban sites could lead to large optical extinctions due to hygroscopic aerosol growth, especially in summer when the relative humidity is often high. In a related study, Zhang et al. (2018) found a large AOD of 1.10 at Wuhan in central China and that was linked to secondary aerosol formation under the high summertime temperatures. Li et al. (2015) similarly concluded that high temperature and humidity promoted the formation of fine particles and led to hygroscopic aerosol growth at Nanjing. Qin et al. (2017) observed a high $AOD_{500\ nm}$ of 1.04 at Shijiazhuang and related this to the hygroscopic growth of aerosol fine-mode particles during polluted days.

Clear spatial variability in EAE values over China is evident in Fig. 3, and at the remote sites, the average EAEs were 1.03. The EAE at Lhasa (0.77) was lower than at Akedala (EAE = 1.13), which is in an arid region of central Asia, or at Shangri-La (EAE = 1.19) in Tibet. The average coarse-mode average effective radii (R_{effC}) at Lhasa was 2.26 μm and the fractional volume was 0.04 $\mu m^3/\mu m^2$, this result suggests the major components of the large mineral dust particles in aerosol populations over that region. The smaller sphericity fraction (~42.70) and lower FMF (0.66) at Lhasa indications the presence of non-spherical aerosol coarse particles compared with the spherical fine particles in the urban sites.

At the arid and semi-arid sites in China, the average EAE value (0.71) was relatively low and the FMF also was low (0.58). The EAE was extremely low at Tazhong (0.25), which is in the Takliman Desert in the Xinjiang Uygur Autonomous Region of northwestern China and the sphericity fraction (12.87)

and FMF (0.35) there were lower compared with most of the other sites. This finding indicates a strong contribution of large particles in this desert region consistent with large volume of the coarse-mode particles (0.27 $\mu m^3/\mu m^2$) noted in section 3.1. The average EAE reached 0.93 at the rural sites near the CLP, and the average value of FMF for those sites was 0.73. Eck et al. (2005) found especially low EAE values in March and April (0.3 and 0.4, respectively) at Yulin, China, where the dust aerosol dominated the optical column.

Large EAEs (1.23) were found at the sites in eastern China, and the FMFs also were large (0.89) at those sites. This result can be attributed to the strong impacts of anthropogenic in the more urbanized eastern part of the country. On the other hand, large EAE values also occurred at the clean sites in northeastern China, including Mt. Longfeng (1.38), where the sphericity fraction was 58.5 and the FMF 0.90. This shows that small particles can have stronger effects in these areas relative to some other regions of China. The EAE at Lin'an was larger than that at Shangdianzi in the Northern Plain or Longfengshan in Northeastern China for most months according to data from Che et al. (2009c). At the urban sites, large EAEs were found at sites in southern China, including Nanning (EAE = 1.36, sphericity fraction = 70.12, FMF = 0.95), Panyu (EAE = 1.43, sphericity fraction = 75.55, FMF = 0.93) and Zhuzilin (EAE = 1.45, sphericity fraction = 55.51, FMF = 0.94). This is likely because the large populations and widespread vehicle ownership in those cities led to the dominance of fine-mode particles throughout the year. Cheng et al. (2015) found a uni-modal distribution of EAE centered in 1.1–1.6 with the occurrence frequency about 72%, which indicated an abundance of fine primary particles at Shanghai in eastern China. At the urban Nanjing site, which is in east-central China, small particles were dominant, and the annual average EAE was 1.21 ± 0.28 (Li et al., 2015).

3.3 Spatial distribution of aerosol single-scattering albedo

The spatial distribution of SSA at 440 nm of the 50 CARSNET stations is

shown in Fig. 4. As a frame of reference, Eck et al. (2005) reported that that SSA_{440nm} from the AERONET retrievals were 0.82 to 0.98 globally. We note that SSA_{440nm} values in this range reflect slightly to strongly absorbing aerosols, and these particles originate from multitude sources (Che et al., 2018). The SSA_{440nm}'s decreased from remote/rural to the urban sites and from west to east, which means that there were higher percentages of absorbing particles at the urban and eastern stations. The average SSA_{440nm} at the remote sites was about 0.91, which is indicative of particles with moderate absorption. The absorbing aerosols at the remote sites were more likely mineral dust particles because those sites are less likely to be affected by carbonaceous particles, which also are absorbing, but mainly produced by anthropogenic activities. The SSA_{440nm}'s for the arid and semi-arid sites were 0.89. The relatively high SSA at Tazhong (0.92) was probably due to slightly absorbing, coarse mode dust particles (EAE = 0.25).

A study by Bi et al. (2011) showed that SSAs increased slightly with wavelength when dust was present at the SACOL site. Moderately absorbing particles were found in our study on or near the Chinese Loess Plateau where the SSA_{440nm}'s were typically 0.88 to 0.89. Eck et al. (2005) concluded that the spectral SSA demonstrated effects of dust at Yulin because the SSA increased for wavelengths from 440 to 675 nm. At the rural sites in eastern China, large SSA_{440nm}'s mainly occurred at sites in the YRD affected anthropogenic influences; these include Tonglu (0.93), Xiaoshan (0.93), Xiyong (0.94). Che et al. (2018) found the slightly absorbing particles came from industrial activity and anthropogenic sources at YRD region with the $SSA_{440\ nm}$ between 0.91 to 0.94.

The average value of SSA_{440nm} at the urban sites was 0.90, which indicates that particles with moderate absorption dominated the aerosol populations. Cheng et al. (2015) reported a seasonal range of SSA from 0.88 to 0.91 at Shanghai, with higher values in autumn and winter compared with spring and summer. Lower SSA_{440nm}'s occurred at the urban sites and

industrial regions in northeastern China, such as Shenyang (0.84), Anshan (0.89), Fuhsun (0.84), which indicates that the particles were more strongly absorbing in that region. On the other hand, higher SSA_{440nm}'s were found at urban sites in southern China, including Nanning (0.92), Panyu (0.90) and Zhuzilin (0.96), and this indicates that the particles at those sites were slightly or weakly absorbing.

Moreover, we found that the SSA_{440nm} spatial distribution reflected the percentages of absorbing aerosols at the urban sites both in northern and eastern China. The reports of Dubovik et al. (2000, 2002, 2006) showed that SSA values vary with both particle size and composition, and Su et al. (2017) used the variations in SSA with wavelength to indicate the presence of brown carbon aerosols at Tianjin, a coastal megacity in China. Qin et al. (2017) suggested that the small SSAs found at Shijiazhuang indicated the presence of fine-mode absorbing particles, such as brown carbon. Zhuang et al. (2014) reported that the SSA at the Nanjing urban site ranged from 0.90 to 0.95, and the aerosol was more absorbing in autumn, possibly due to the biomass burning emission in the YRD. As evident in the results presented in section 3.1, one can see that the R_{effT}, R_{effF} and R_{effC} between northeastern and southern China was very similar. For example, at Shenyang, a megacity in northeastern China, the effective radii of total, fine- and coarse-mode particles were 0.31, 0.16, 2.23 μm and the corresponding volumes were 0.22, 0.12, 0.10 $\mu m^3/\mu m^2$, respectively. At Hangzhou in the YRD region, the R_{effT}, R_{effF} and R_{effC} were 0.30, 0.17, 2.21 μm with the volumes about 0.22, 0.12, 0.10 $\mu m^3/\mu m^2$, respectively. Therefore, the different SSA_{440nm} distributions in the two regions may be attributed by the special aerosol composition related to the urban-industrial background of northeastern China (lower SSA440nm) and more anthropogenic sources in the eastern China environmental (higher SSA440nm).

Dust aerosols with light-absorbing occur more frequently in spring in northeastern China than in more southern regions (Zhao et al., 2018).

Anthropogenic emissions from seasonal biomass burning and residential heating are two other main factors that affect aerosol composition between the two regions (Che et al., 2018). Especially in winter, there was high percentage of absorbing aerosols at the northeastern sites, and that was more than likely caused by emissions of carbonaceous aerosol from residential heating (Zhao et al., 2015). Climatic conditions are also the main factors affecting the absorption characteristics of aerosols in different regions of north and south China. The increased light scattering could well be due to the particles hygroscopic growth demonstrated in other studies. For example, Mai et al. (2018) found that AODs and SSAs both increased with relative humidity at Guangdong in the PRD region, which suggests that condensational growth can affect the aerosol optical properties.

3.4 Spatial distributions of absorption aerosol optical depth (AAOD)

The spatial distribution of AAOD at 440 nm shown as Fig. 5 indicates that overall, the $AAOD_{440nm}$'s increased from north to south and from remote/rural to urban sites. Lower $AAOD_{440nm}$'s were found at the remote stations, where the average value was 0.01. The $AAOD_{440nm}$ at Akedala, a remote site in northwestern China, was 0.02, and that was higher than at Shangri-La or Lhasa (0.01), both of which are on the Tibetan Plateau. The low $AAOD_{440nm}$'s throughout that region indicates that the aerosol population was not strongly absorbing. Compared with these three sites, the average $AAOD_{440nm}$'s at the arid and semi-arid sites were higher (0.03); for example, an $AAOD_{440nm}$ of 0.05was found at Tazhong, which is adjacent to the desert, and that indicates that the aerosol particles were more absorbing. As discussed in sections 3.2 and 3.3, dust aerosols likely make a significant contribution to aerosol light absorption in the areas impacted by the deserts.

The low $AAOD_{440nm}$ found at Xilinhot (0.02) was probably due to the low aerosol loadings (AOD_{440nm} = 0.21) in this region. The $AAOD_{440nm}$'s at the Mt. Gaolan and Yulin rural sites which on or around the CLP were about 0.04 and

0.03, respectively, and the particles were moderately absorbing (SSA = 0.89). The large $AAOD_{440nm}$ at Datong (0.09) can be explained by the high AOD_{440nm} (0.58) there. Indeed, large $AAOD_{440nm}$'s were found at rural sites in eastern China, where there were high AODs and low SSAs as noted in sections 3.2 and 3.3. Of these sites, Dengfeng (AOD_{440nm} = 0.08) and Huimin (AOD_{440nm} = 0.08) are located on the North China Plain, while Huainan (AOD_{440nm} = 0.10) is on the Guanzhong Plain. Lower $AAOD_{440nm}$'s, from 0.02–0.03, occurred at Tongyu (0.03), which is at a semi-arid region in northeastern China, at the Mt. Longfeng (0.03) regional background site on the Northeast China Plain, at the Yushe rural site in northern China (0.03), and at the clean Xiyong site in the PRD (0.02).

Several urban sites showed $AAOD_{440nm}$ values greater than 0.10; these include Fushun (0.11) and Shenyang (0.14) in the northeastern China, Lanzhou (0.10) in the northwestern China, and Nanjing (0.10) and Wuhan (0.11) in the eastern and central China. Lower $AAOD_{440nm}$'s occurred in other urban areas, such as Yinchuan ($AAOD_{440nm}$ = 0.02, AOD_{440nm} = 0.37) in the northwest and Zhuzilin ($AAOD_{440nm}$ = 0.03, AOD_{440nm} = 0.66) in the PRD; both of these sites had relatively low AOD_{440}'s indicating weaker anthropogenic influences compared with metropolitan regions of some other areas. We note that there are significant uncertainties in relating aerosol absorbing properties to particle types, such as black carbon, organic matter, as well as mineral dust (Russell et al., 2010; Giles et al., 2012). Nonetheless, the information presented here on the spatial distribution of AAODs over China may be useful for the further investigations into the relationships between light absorption and particle type (Liu et al., 2017; Schuster et al., 2016a, 2016b).

3.5 Spatial distribution of direct aerosol radiative effect at the Earth's surface and top of the atmosphere

The spatial distributions of the DAREs calculated for both the bottom and top of the atmosphere are shown in Fig. 6. Overall, the DARE-BOAs increased

563 from northwest to southeast and from rural to urban sites, consistent with
564 impacts from the densely populated regions around the sites. The average
565 DARE-BOA at the remote sites was -24.40 W/m^2, and in comparison, a higher
566 DARE-BOA (-33.65 W/m^2) occurred at Akedala, which occurred on a remote
567 region of northwestern China. The AOD_{440nm} at Akedala was relatively low
568 (0.17) and the SSA moderate (0.90). The moderate absorption of aerosol could
569 lead to more strong surface cooling effects with little higher DARE-BOA than
570 the other remote sites. The DARE-BOAs for Lhasa and Shangri-La were
571 -22.13 and -17.43 W/m^2, respectively. These results indicate weaker surface
572 cooling effects at the remote sites relative to other regions because the aerosol
573 loadings were relatively low, as indicated by AOD_{440nm}'s < 0.20.

574 The average DARE-BOTs at the arid and semi-arid sites of China were
575 about -56.43 W/m^2, and those high DARE-BOAs can be explained by the
576 moderately absorbing particles (SSA = 0.89) and large AOD_{440nm}'s (0.32)
577 compared with the remote sites. A large DARE-BOA (-91.20 W/m^2) occurred at
578 the Tazhong site near the northwestern deserts, and there, the high AOD (0.60)
579 and the slight absorption of mineral dust (SSA = 0.92) imply substantial surface
580 cooling. The average DARE-BOA for rural sites on the Chinese Loess Plateau
581 or surrounding was -74.67 W/m^2, and that also implies cooling at the surface.

582 Several rural sites in northern and eastern China had large DARE-BOA
583 values; these include Huimin (-111.58 W/m^2), Dengfeng (-104.78 W/m^2) and
584 Huainan (-129.17 W/m^2), and at those sites the AODs were high, from 0.80–
585 0.90, and the SSAs were ~0.89. These results show stronger surface cooling
586 effects at sites influenced by anthropogenic emissions compared with the
587 remote sites or those near the deserts. The large negative DARE-BOA values
588 (-103.28 W/m^2) at the urban sites indicate that the combination of high
589 AOD_{440nm}'s (0.79) and moderate SSAs (0.90) can cause significant surface
590 cooling. Indeed, anthropogenic emissions presumably led to the high
591 DARE-BOAs at urban sites, including Shenyang (-144.88 W/m^2) and Fushun
592 (-116.91 W/m^2) in the Northeastern Plain, Xian in the Guanzhong Plain

(-132.55 W/m^2), Chengdu in the Sichuan Basin (-110.42 W/m^2), Lanzhou in the western region (-126.17 W/m^2), and Nanjing (-143.38 W/m^2) and Wuhan (-171.80 W/m^2) in the Central China. These results indicate that anthropogenic aerosols can cause significant direct radiative effects at urban sites.

The DARE-TOAs increased from north to south and from rural to urban sites, and the average DARE-TOA for the remote stations was low, about -4.79 W/m^2 (Fig. 7). The DARE-TOAs at Lhasa and Shangri-La were -5.04 W/m^2 and -8.93 W/m^2, respectively. A notably small DARE-TOA was found at Akedala (-0.42 W/m^2), indicating that the effects of the aerosol on the temperature of earth-atmosphere system there would be weak. The average DARE-TOA at the arid and semi-arid sites was -10.17 W/m^2. The large DARE-TOA found at Tazhong (-23.49 W/m^2) could represent the larger contribution of slightly absorbing mineral aerosols (SSA = 0.92) and a large AOD (0.60); this indicates more cooling at surface through the absorption and scattering solar radiation compared with the less impacted sites. This is consistent with the results for Tazhong discussed in section 3.1 which showed high volumes of coarse mode particles with large radii.

The average DARE-TOA at rural sites on the Chinese Loess Plateau or nearby was about -14.56 W/m^2. Although the SSA_{440nm} were close to Gaolan and Yulin about 0.89, the TOAs were quite different (Mt. Gaolan -20.87 W/m^2; Yulin -9.09 W/m^2) which could be due to the different AOD_{440nm} about 0.36 and 0.32, respectively. In rural eastern China, the DARE-TOA was about -32.40 W/m^2, and to put this in context, Che et al. (2018) found that DARE-TOAs of −40 W/m^2 at rural sites in the YRD region, which is indicative of a relatively strong cooling effect. Low DARE-TOAs were found at the Mt. Longfeng rural site in northeastern China (DARE-TOA = -11.34, AOD_{440nm} = 0.34, SSA = 0.89) and at the Tongyu semi-arid site in northeastern China as (DARE-TOA = -8.87, AOD_{440nm} = 0.23, SSA = 0.88) where the aerosol loadings were relatively low and the absorption was moderate.

In the urban sites at central and eastern China, the average DARE-TOA

values were about -30.05 W/m^2. Higher DARE-TOAs occurred at Anshan in the Northeastern Plain (-39.66 W/m^2), Chengdu in the Sichuan Basin (-52.21 W/m^2), Hangzhou in the YRD (-40.16 W/m^2), Jiaozuo (-39.35 W/m^2) and Zhengzhou (-46.18 W/m^2) in the North China Plain, and Zhuzilin (-40.15 W/m^2) in the PRD region. The high DARE-TOA values at these urban sites imply relatively strong cooling effects due to higher aerosol loadings in the atmosphere.

3.6 Spatial distributions of aerosol mixing properties

The spatial distribution of aerosol mixing properties (Figure 8) was obtained by using the SSA_{440nm}, FMF, and EAE results to classify the particles based on size and absorbing properties. In previous studies by Zheng et al. (2017) and Che et al. (2018), the particles in this study were grouped into eight types as Table 2 show. Moreover, the FMF has been provided to give the particle size information in the group of the particles.

At the remote Akedala and Lhasa sites (FMF = 0.70–0.78 and SSA_{440nm} = 0.85), the percentages of mixed absorbing particles (Type V) were 35-40%, while at Shangri-la (FMF = 0.76, SSA_{440nm} = 0.84), the percentage was slightly lower, 24.62%. The characteristics of the particles at these remote, high-altitude sites were probably affected by the rugged topography which would promote particle mixing. The proportion of coarse mode, mainly dust, particles with moderate to strong absorption (Group VII) was highest at the arid and semi-arid sites. The percent abundances of Group VII particles were 57.90% at Dunhuang (AE = 0.26, SSA_{440nm} = 0.85, FMF = 0.43) and 58.52% at Tazhong (AE = 0.20, SSA_{440nm}= 0.87, FMF = 0.37), respectively. Mixed absorbing particles (Type V) and strongly absorbing dust particles (Group VII) accounted for 30 to 70% of the aerosol in the rural sites on or near the CLP. The percentages of mixed absorbing particles (Type V) at Gaolan, Yulin, and Datong were 31.98%, 45.22% and 29.04%, respectively, and the average FMFs at those sites ranged from 0.70–0.76.

653 The proportions of the coarse-mode aerosols with strongly absorbing in
654 Group VII were about 35.23% at Gaolan and 21.21% at Yulin, which was
655 mainly dust particles with the FMFs at those sites were 0.43 and 0.48,
656 respectively. The proportion of coarse-mode particles with strongly absorbing
657 in Group VII and coarse-mode particles with weakly-absorbing in Group VIII at
658 the rural sites in eastern China were < 11%. These patterns indicated that the
659 differences in the eastern region from northwestern China because in the east,
660 coarse-mode particles have only a minor contribution to aerosol absorption.
661 The percentage of fine-mode particles with weakly-absorbing in Type IV and
662 mixed absorbing particles in Type V combined about ~50% at the eastern sites.
663 This result suggests that mixed aerosols originated from a variety of sources
664 and that many of the sites were affected by anthropogenic emissions from
665 megacities upwind.

666 The fine-mode particles with absorbing in Types I, II, III and V accounted
667 for 50 to 90% at most of the urban sites. The percentages of these four particle
668 types combined were especially large in eastern China; for example, at Panyu,
669 particle Types I—IV composed 90.83% of the total, and the FMF there was
670 0.90–0.94, while at Zhuzilin, the percentage of Types I–IV was 92.55%, and
671 the FMF was 0.92–0.94. These results are another indication that fine-mode
672 particles are important for light absorption in urban areas. In contrast, the
673 Lanzhou and Urumqi urban sites were less affected by absorbing fine-particles
674 because the percentages of Type I–IV particles were only 19.73% and 18.36%,
675 respectively. The mixed absorbing Type V particles accounted for large
676 percentages of the total at Lanzhou (48.80%, EAE = 0.88, SSA = 0.82, FMF =
677 0.73) and at Urumqi (59.39%, EAE = 0.94, SSA = 0.84, FMF = 0.75). Different
678 from the other urban sites, these patterns show that larger particles had
679 significant contributions to the aerosol absorption at these two northwestern
680 sites.

681

682 **4. Conclusions**

683 Aerosol microphysical and its optical properties obtained from the
684 ground-based sunphotometer deployed at 50 CARSNET stations were used to
685 begin the development of their climatology characteristics and to investigate
686 potential aerosol-climate effects over vast area of China. Direct aerosol
687 radiative effects (DAREs) at the bottom and at the top of the atmosphere were
688 calculated, and eight types of aerosols were classified based on the particle
689 size and absorbing properties. The annual mean values of the ReffT
690 decreased from the arid and semi-arid sites (0.55 μm) to the urban sites (0.37
691 μm). The aerosol volumes increased from the remote sites (0.05 $\mu m^3/\mu m^2$) to
692 the urban sites (0.21 $\mu m^3/\mu m^2$). The volumes of coarse-mode particle were
693 larger than those for the fine mode at the remote and arid/semi-arid sites—this
694 can be explained by the greater relative abundances of mineral dust compared
695 with pollution-derived particles at those sites. At the urban sites, where
696 anthropogenic influences were relatively strong, the proportion of fine mode
697 particles increased gradually with aerosol volume.

698 The AOD_{440nm} progressively increased from the remote sites (0.12) to the
699 arid and semi-arid sites (0.32) to rural sites in eastern China (0.70) and finally
700 to the urban sites (0.79), which were the ones most strongly affected by
701 anthropogenic activities. The average $EAE_{440\text{-}870\ nm}$'s at the arid and semi-arid
702 sites were relatively low (0.71), which indicates an important contribution of
703 larger particles to the aerosol extinction in those regions. The consistently
704 large $EAE_{440\text{-}870\ nm}$'s at the urban sites (> 1.20) and the high FMFs that those
705 site (0.88) are the evidence that fine mode particles are prevalent throughout
706 year. The average SSA_{440nm}'s at the remote, rural, and urban sites were
707 relatively similar, averaging about 0.89, and this indicates the particles were
708 moderately absorbing.

709 Overall, dust aerosols with light-absorbing in spring and emissions came
710 from biomass burning and residential heating during the colder months were
711 the main factors that led to spatial differences in the percentages of absorbing
712 aerosols over China. The $AAOD_{440nm}$'s increased from the remote sites (0.01)

to the arid and semi-arid sites (0.03) to the rural sites of eastern China (0.05) and finally to the urban sites (0.07). High $AAOD_{440nm}$'s were caused by light-absorbing dust aerosols at the rural sites and by the strong anthropogenic emissions in the metropolitan areas. The spatial patterns in the absorbing aerosols were not only affected by the chemical composition of aerosol, but also by physical effects imposed by topography, weather, and climate.

The average DARE-BOA values were -24.40 W/m^2 at the remote sites; -56.43 W/m^2 at the arid and semi-arid sites; -74.67 W/m^2 at the sites on the CLP or nearby; -85.25 W/m^2 at the rural sites in eastern China; and -103.28 W/m^2 at the urban sites. The larger DARE-BOA values at the urban sites imply stronger cooling effects from anthropogenic emissions compared with those from mineral dust at the remote sites or those near the desert. Moreover, larger DARE-TOA's also occurred at the urban sites (-30.05 W/m^2), which indicates strong cooling effects due to the large aerosol extinctions between the earth-atmosphere system displayed the moderate to strong light absorption. Mixed-absorbing particles were the most abundant aerosol type in the remote and rural sites on or near the Chinese Loess Plateau and in eastern China. Mineral dust particles with moderate to strong absorbing were dominant in the arid and semi-arid sites while absorbing fine-mode particles accounted for 50 to 90% of the aerosol at the most urban sites.

The results of the study have considerable value for ground truthing satellite observations and for validating aerosol models. Moreover, the results also have provided significant information on aerosol optical and radiative properties for different types of sites covering a broad expanse of China. These results also are a major step towards developing a climatology for aerosol microphysical and optical properties for China and even East Asia.

Data availability:

The detailed CARSNET AOD dataset used in the study can be requested by contacting the corresponding author.

Competing interests.

743 The authors declare that they have no conflict of interest.

744 **Author contribution:**

745 All authors contributed to shaping up the ideas and reviewing the paper.
746 HC, XX and XZ designed and implemented the research, as well as prepared
747 the manuscript; HC, HZ,YW and HW contributed to analysis of the CARSNET
748 dataset; HC, XX, JZ, OD, BNH, PG, and ECA contributed to the CARSNET
749 data retrieval; HC, BQ, WG, HY, RZ, LY, JC, YZ, KG, and XZ carried out the
750 CARSNET observations; OD, BNH, PG, and ECA provided constructive
751 comments on this research.

752 **Acknowledgments**

753 This work was supported by grants from the National Science Fund for
754 Distinguished Young Scholars (41825011), the National Key R & D Program
755 Pilot Projects of China (2016YFA0601901), National Natural Science
756 Foundation of China (41590874), the CAMS Basis Research Project
757 (2017Z011), the European Union Seventh Framework Programme
758 (FP7/2007-2013) under grant agreement no. 262254. AERONET-Europe
759 ACTRIS-2 program, European Union's Horizon 2020 research and innovation
760 programme under grant agreement No 654109.

761

762 **References**

763 Bi, J.R., Huang, J.P., Fu, Q., Wang, X., Shi, J.S., Zhang, W., Huang, Z.W., and
764 Zhang, B.D.: Toward characterization of the aerosol optical properties
765 over Loess Plateau of Northwestern China, Journal of Quantitative
766 Spectroscopy and Radiative Transfer, 112, 346-360,
767 https://doi.org/10.1016/j.jqsrt.2010.09.006, 2011.

768 Bokoye, A.I., Royer, A., O'Neill, N.T., Cliche, P., Fedosejevs, G., Teillet, P.M.,
769 and Mcarthur, L.J.B.: Characterization of atmospheric aerosols across
770 Canada from a Ground-based sun photometer network: Aerocan, Atmos.
771 Ocean., 39, 429–456, https://doi.org/10.1080/07055900.2001.9649687,
772 2001.

773 Breon, F., Tanré, D., and Generoso, S.: Aerosols effect on the cloud droplet
774 size monitored from satellite, Science, 295, 834-838,
775 https://doi.org/10.1126/science.1066434, 2002.
776 Cao, J.J., Lee, S.C., Chow, J.C., Watson, J.G., Ho, K.F., Zhang, R.J., Jin, Z.D.,
777 Shen, Z.X., Chen, G.C., Kang, Y.M., Zou, S.C., Zhang, L.Z., Qi, S.H., Dai,
778 M.H, Cheng, Y., and Hu, K.: Spatial and seasonal distributions of
779 carbonaceous aerosols over China, J. Geophys. Res., 112, D22S11.
780 http://dx.doi.org/10.1029/2006JD008205, 2007.
781 Charlson, R. J., Schwartz, S. E., Hales, J. M., Cess, D., Coakley, J. A., and
782 Hansen, J. E.: Climate forcing by anthropogenic aerosols, Science, 255,
783 423–430, https://doi.org/10.1126/science.255.5043.423, 1992.
784 Che, H.Z., Shi, G.Y., Zhang, X.Y., Arimoto, R., Zhao, J.Q., Xu, L., Wang, B.,
785 and Chen, Z.H.: Analysis of 40 years of solar radiation data from China,
786 1961-2000, Geophysical Research Letters, 32, L06803,
787 https://doi.org/10.1029/2004GL022322, 2005.
788 Che, H., Shi, G., Uchiyama, A., Yamazaki, A., Chen, H., Goloub, P., and Zhang,
789 X.: Intercomparison between aerosol optical properties by a PREDE
790 skyradiometer and CIMEL sunphotometer over Beijing, China, Atmos.
791 Chem. Phys., 8, 3199–3214, http://dx.doi.org/10.5194/acp-8-3199-2008,
792 2008.
793 Che, H., Zhang, X., Chen, H., Damiri, B., Goloub, P., Li, Z., Zhang, X., Wei, Y.,
794 Zhou, H., Dong, F., Li, D., and Zhou, T.: Instrument calibration and aerosol
795 optical depth (AOD) validation of the China Aerosol Remote Sensing
796 Network (CARSNET), J. Geophys. Res., 114, D03206,
797 https://doi.org/10.1029/2008JD011030, 2009a.
798 Che, H. Z., Zhang, X. Y., Alfraro, S., Chatenet, B., Gomes, L., and Zhao, J. Q.:
799 Aerosol optical properties and its radiative forcing over Yulin, China in
800 2001 and 2002, Adv. Atmos. Sci., 26, 564–576,
801 https://doi.org/10.1007/s00376-009-0564-4, 2009b.
802 Che, H. Z., Yang, Z. F., Zhang, X. Y., Zhu, C. Z., Ma, Q. L., Zhou, H. G., and

Wang, P.: Study on the aerosol optical properties and their relationship with aerosol chemical compositions over three regional background stations in China, Atmospheric Environment, 43, 1093–1099, https://doi.org/10.1016/j.atmosenv.2008.11.010, 2009c.

Che, H., Xia, X., Zhu, J., Li, Z., Dubovik, O., Holben, B., Goloub, P., Chen, H., Estelles, V., Cuevas-Agulló, E., Blarel, L., Wang, H., Zhao, H., Zhang, X., Wang, Y., Sun, J., Tao, R., Zhang, X., and Shi, G.: Column aerosol optical properties and aerosol radiative forcing during a serious haze-fog month over North China Plain in 2013 based on ground-based sunphotometer measurements, Atmos. Chem. Phys., 14, 2125–2138, https://doi.org/10.5194/acp-14-2125-2014.

Che, H., Zhang, X.-Y., Xia, X., Goloub, P., Holben, B., Zhao, H., Wang, Y., Zhang, X.-C., Wang, H., Blarel, L., Damiri, B., Zhang, R., Deng, X., Ma, Y., Wang, T., Geng, F., Qi, B., Zhu, J., Yu, J., Chen, Q., and Shi, G.: Ground-based aerosol climatology of China: aerosol optical depths from the China Aerosol Remote Sensing Network (CARSNET) 2002–2013, Atmos. Chem. Phys., 15, 7619–7652, https://doi.org/10.5194/acp-15-7619-2015, 2015.

Che, H., Qi, B., Zhao, H., Xia, X., Eck, T.F., Goloub, P., Dubovik, O., Estelles, V., Cuevas-Agulló, E., Blarel, L., Wu, Y., Zhu, J., Du, R., Wang, Y., Wang, H., Gui, K., Yu, J., Zheng, Y., Sun, T., Chen, Q., Shi, G., and Zhang X.: Aerosol optical properties and direct radiative forcing based on measurements from the China Aerosol Remote Sensing Network (CARSNET) in eastern China, Atmospheric Chemistry and Physics, 18, 405–425, https://doi.org/10.5194/acp-18-405-2018, 2018.

Cong, Z.Y., Kang, S.C., Liu, X.D., and Wang, G.F.: Elemental composition of aerosol in the Nam Co region, Tibetan Plateau, during summer monsoon season, Atmospheric Environment, 41, 1180–1187, https://doi.org/10.1016/j.atmosenv.2006.09.046, 2007.

Cong, Z.Y., Kang, S.C., Smirnov, A., and Holben, B.: Aerosol optical properties

833 at Nam Co, a remote site in central Tibetan Plateau, Atmospheric
834 Research, 92, 42–48, https://doi.org/10.1016/j.atmosres.2008.08.005,
835 2009.
836 Duan, J. and Mao, J.: Study on the distribution and variation trends of
837 atmospheric aerosol optical depth over the Yangtze River Delta, Acta
838 Scien. Circum., 27, 537–543,
839 https://doi.org/10.1007/978-1-4020-6475-3_126, 2007.
840 Dubovik, O. and King, M. D.: A flexible inversion algorithm for retrieval of
841 aerosol optical properties from sun and sky radiance measurements, J.
842 Geophys. Res., 105, 20673–20696,
843 https://doi.org/10.1029/2000JD900282, 2000.
844 Dubovik, O., Holben, B. N., Eck, T. F., Smirnov, A., Kaufman, Y. J., King, M. D.,
845 Tanre, D., and Slutsker, I.: Variability of absorption and optical properties
846 of key aerosol types observed in worldwide locations, J. Atmos. Sci., 59,
847 590–608,
848 https://doi.org/10.1175/1520-0469(2002)059<0590:VOAAOP>2.0.CO;2,
849 2002.
850 Dubovik, O., Sinyuk, A., Lapyonok, T., Holben, B. N., Mishchenko, M., Yang, P.,
851 Eck, T. F., Volten, H., Munoz, O., Veihelmann, B., van der Zande, W. J.,
852 Leon, J. F., Sorokin, M., and Slutsker, I.: Application of spheroid models to
853 account for aerosol particle nonsphericity in remote sensing of desert dust,
854 J. Geophys. Res.-Atmos., 111, D11208,
855 https://doi.org/10.1029/2005JD006619, 2006.
856 Dubuisson, P., Buriez, J. C., and Fouquart, Y.: High spectral resolution solar
857 radiative transfer in absorbing and scattering media, application to the
858 satellite simulation, J. Quant. Spectrosc. Ra., 55, 103–126,
859 https://doi.org/10.1016/0022-4073(95)00134-4, 1996.
860 Eck, T. F., Holben, B. N., Reid, J. S., Dubovik, O., Smirnov, A., O'Neill, N. T.,
861 Slutsker, I., and Kinne, S.: Wavelength dependence of the optical depth of
862 biomass burning, urban, and desert dust aerosols, J. Geophys. Res., 104,

31333–31349, https://doi.org/10.1029/1999jd900923, 1999.

Eck, T. F., Holben, B. N., Dubovik, O., Smirnov, A., Goloub, P., Chen, H. B., Chatenet, B., Gomes, L., Zhang, X. Y., Tsay, S. C., Ji, Q., Giles, D., and Slutsker, I.: Columnar aerosol optical properties at AERONET sites in central eastern Asia and aerosol transport to the tropical Mid-Pacific, J. Geophys. Res., 110, D06202, https://doi.org/10.1029/2004JD005274, 2005.

Estellés, V., Campanelli, M., Utrillas, M. P., Expósito, F., and Martínez-Lozano, J. A.: Comparison of AERONET and SKYRAD4.2 inversion products retrieved from a Cimel CE318 sunphotometer, Atmos. Meas. Tech., 5, 569–579, https://doi.org/10.5194/amt-5-569-2012, 2012.

Fan, X., Chen, H., Goloub, P., Xia, X., Zhang, W., and Chatenet, B.: Analysis of column-integrated aerosol optical thickness in Beijing from AERONET observations, China Particuol., 4, 330-335, DOI: 10.1016/s1672-2515(07)60285-1, 2006.

García, O. E., Díaz, J. P., Expósito, F. J., Díaz, A. M., Dubovik, O., Dubuisson, P., Roger, J.-C., Eck, T. F., Sinyuk, A., Derimian, Y., Dutton, E. G., Schafer, J. S., Holben, B. N., and García, C. A.: Validation of AERONET estimates of atmospheric solar fluxes and aerosol radiative forcing by groundbased broadband measurements, J. Geophys. Res., 113, D21207, https://doi.org/10.1029/2008JD010211, 2008.

García, O. E., Díaz, J. P., Expósito, F. J., Díaz, A. M., Dubovik, O., and Derimian, Y.: Aerosol radiative forcing: AERONET based estimates, climate Models, InTech, edited by: Druyan, L., ISBN: 978- 953-51-0135-2, 2012.

Garrett, T. J., and Zhao, C.: Increased Arctic cloud longwave emissivity associated with pollution from mid-latitudes, Nature, 440, 787-789, doi:10.1038/nature04636, 2006.

Gelencser, A.: Carbonaceous Aerosol, Atmospheric and Oceanographic Sciences Libery., vol. 30. Springer, Netherland., 2004.

Giles, D. M., Holben, B. N., Tripathi, S. N., Eck, T. F., Newcomb, W. W., Slutsker, I., Dickerson, R. R., Thompson, A. M., Mattoo, S., Wang, S., Singh, R. P., Sinyuk, A., and Schafer, J. S.: Aerosol properties over the Indo-Gangetic Plain: A mesoscale perspective from the TIGERZ experiment, J. Geophys. Res.-Atmos., 116(D18), DOI: 10.1029/2011JD015809, 2011.

Giles, D. M., Holben, B. N., Eck, T. F., Sinyuk, A., Smirnov, A., Slutsker, I., Dickerson, R. R., Thompson, A. M., and Schafer, J. S.: An analysis of AERONET aerosol absorption properties and classifications representative of aerosol source regions, J. Geophys. Res.-Atmos., 117, 127–135, DOI: 10.1029/2012JD018127, 2012.

Gobbi, G. P., Kaufman, Y. J., Koren, I., and Eck, T. F.: Classification of aerosol properties derived from AERONET direct sun data, Atmos. Chem. Phys., 7, 453–458, http://dx.doi.org/10.5194/acp-7-453-2007, 2007

Goloub, P., Li, Z., Dubovik, O., Blarel, L., Podvin, T., Jankowiak, I., Lecoq, R., Deroo, C., Chatenet, B., and Morel, J. P.: PHOTONS/AERONET sunphotometer network overview: description, activities, results, Fourteenth International Symposium on Atmospheric and Ocean Optics/Atmospheric Physics, 6936, 69360V, DOI: 10.1117/12.783171, 2007.

Haywood, J. M. and Shine, K. P.: The effect of anthropogenic sulfate and soot aerosol on the clear sky planetary radiation budget, Geophys. Res. Lett., 22, 603–606, https://doi.org/10.1029/95GL00075, 1995.

He, Q., Li, C., Geng, F., Yang, H., Li, P., Li, T., Liu, D., and Pei, Z.: Aerosol optical properties retrieved from Sun photometer measurements over Shanghai, China, J. Geophys. Res.-Atmos., 117, D16204, https://doi.org/10.1029/2011JD017220, 2012.

Holben, B. N., Eck, T. F., Slutsker, I., Tanré, D., Buis, J. P., Setzer, A., Vermote, E., Reagan, J. A., Kaufman, Y. J., Nakajima, T., Lavenu, F., Jankowiak, I., and Smirnov, A.: AERONET – A Federated Instrument Network and Data

923 Archive for Aerosol Characterization, Remote Sens. Environ., 66, 1–16,
924 https://doi.org/10.1016/S0034-4257(98)00031-5, 1998.
925 Jacobson, M. Z.: A physically based treatment of elemental carbon optics:
926 implications for global direct forcing of aerosols, Geophys. Res. Lett., 27,
927 217–220, DOI: 10.1029/1999gl010968, 2000.
928 Lacis, A. A. and Oinas, V.: A description of the correlated kdistribution method
929 for modeling nongray gaseous absorption, thermal emission, and multiple
930 scattering in vertically inhomogeneous atmospheres, J. Geophys. Res.,
931 96, 9027–9063, DOI: 10.1029/90JD01945, 1991.
932 Lee, K. H., Li, Z., Cribb, M. C., Liu, J., Wang, L., Zheng, Y., Xia, X., Chen, H.,
933 and Li, B.: Aerosol optical depth measurements in eastern China and a
934 new calibration method, J. Geophys. Res., 115, 4038–4044,
935 https://doi.org/10.1029/2009JD012812, 2010.
936 Li, C.C., Mao, J.T., Lau, A.K.H., Chen, J.C., Yuan, Z.B., Liu, X.Y., Zhu, A.H.,
937 and Liu, G.Q.: Characteristics of distribution and seasonal variation of
938 aerosol optical depth in eastern China with MODIS products, Chinese
939 Science Bulletin., 48, 2488-2495, DOI: 10.1360/03wd0224, 2003.
940 Li, Z., Chen, H., Cribb, M., Dickerson, R., Holban, B., Li, C., Lu, D., Luo, Y.,
941 Maring, H., Shi, G., Tsay, S.C., Wang, P., Wang, Y., Xia, X., and Zhao, F.:
942 Overview of the East Asian Studies on tropospheric aerosols, an
943 international regional experiment(EAST-AIRE), J. Geophys. Res., 112,
944 D22S00. http://dx.doi.org/10.1029/2007JD008853, 2007.
945 Li, X., and Zhang, L.: Analysis of aerosol sources and optical properties based
946 on backward trajectory method over SACOL, Acta Physica Sin., 61, 1-9,
947 DOI: 10.7498/aps.61.023402, 2012.
948 Li, Z. Q., Eck, T., Zhang, Y., Zhang, Y. H., Li, D. H., Li, L., Xu, H., Hou, W. Z., Lv,
949 Y., Goloub, P., and Gu, X. F.: Observations of residual submicron fine
950 aerosol particles related to cloud and fog processing during a major
951 pollution event in Beijing, Atmos. Environ., 86, 187–192, DOI:
952 10.1016/j.atmosenv.2013.12.044, 2014.

Li, Z., Lau, W. K.-M., Ramanathan, V., Wu, G., Ding, Y., Manoj, M. G., Liu, J., Qian, Y., Li, J., Zhou, T., Fan, J., Rosenfeld, D., Ming, Y., Wang, Y., Huang, J., Wang, B., Xu, X., Lee, S.- S., Cribb, M., Zhang, F., Yang, X., Takemura, T., Wang, K., Xia, X., Yin, Y., Zhang, H., Guo, J., Zhai, P. M., Sugimoto, N., Babu, S. S., and Brasseur, G. P.: Aerosol and monsoon climate interactions over Asia, Rev. Geophys., 54, 866–929, https://doi.org/10.1002/2015RG000500, 2016.

Li, Z.Q., Xu, H., Li, K. T., Li, D. H., Xie, Y. S., Li, L., Zhang, Y., Gu, X.F., Zhao, W., Tian, Q.J., Deng, R.R., Su, X.L., Huang, B., Qiao, Y.L., Cui, W.Y., Hu, Y., Gong, C.L., Wang, Y.Q., Wang, X.F., Wang, J.P., Du, W.B., Pan, Z.Q., Li, Z.Z., and Bu, D.: Comprehensive Study of Optical, Physical, Chemical, and Radiative Properties of Total Columnar Atmospheric Aerosols over China: An Overview of Sun–Sky Radiometer Observation Network (SONET) Measurements, Bulletin of the American Meteorological Society., 99(4), 739–755, https://doi.org/10.1175/BAMS-D-17-0133.1, 2018.

Luo, Y., Lu, D., Zhou, X., and Li, W.: Analyses on the spatial distribution of aerosol optical depth over china in recent 30 years, Chinese Journal of Atmospheric Sciences., 26, 721-730, DOI: 10.1002/mop.10502, 2002.

Mai, B., Deng, X., Xia, X., Che, H., Guo, J., Liu, X., Zhu, J., and Ling, C.: Column-integrated aerosol optical properties of coarse- and fine-mode particles over the Pearl River Delta region in China, Sci. Total. Environ., 622–623, 481-492, DOI: 10.1016/j.scitotenv.2017.11.348, 2018.

Myhre, G.: Consistency between satellite-derived and modeled estimates of the direct aerosol effect, Science, 325, 187-190, DOI: 10.1126/science.1174461, 2009.

Nakajima, T. and Tanaka, M.: Algorithms for radiative intensity calculations in moderately thick atmospheres using a truncation approximation, J. Quant. Spectrosc. Ra., 40, 51–69, https://doi.org/10.1016/0022-4073(88)90031-3,1988.

Pappalardo, G., Amodeo, A., Apituley, A., Comeron, A., Freudenthaler, V.,

983 Linné, H., Ansmann, A., Bösenberg, J., D'Amico, G., Mattis, I., Mona, L.,
984 Wandinger, U., Amiridis, V., AladosArboledas, L., Nicolae, D., and
985 Wiegner, M.: EARLINET: towards an advanced sustainable European
986 aerosol lidar network, Atmos. Meas. Tech., 7, 2389–2409,
987 https://doi.org/10.5194/amt- 7-2389-2014, 2014.
988 Prats, N., Cachorro, V. E., Berjón, A., Toledano, C., and De Frutos, A. M.:
989 Column-integrated aerosol microphysical properties from AERONET Sun
990 photometer over southwestern Spain, Atmos. Chem. Phys., 11, 12535–
991 12547, DOI:10.5194/acp-11- 12535-2011, 2011.
992 Qin, K., Wang, L.Y., Wu, L.X., Xu, J., Rao, L.L., Letu, H., Shi, T.W., Wang, R.F.,
993 2017. A campaign for investigating aerosol optical properties during winter
994 hazes over Shijiazhuang, China, Atmos. Res., 198, 113-122,
995 https://doi.org/10.1016/j.atmosres.2017.08.018, 2017.
996 Ramanathan, V., Crutzen, P. J., Kiehl, J. T., and Rosenfeld, D.: Aerosol,
997 climate, and hydrological cycle, Science 294, 2119–2124,
998 https://doi.org/10.1126/science.1064034, 2001.
999 Remer, L. A., and Kaufman, Y. J.: Dynamic aerosol model: Urban/industrial
1000 aerosol, J. Geophys. Res., 103, 13859–13871,
1001 https://doi.org/10.1029/98jd00994, 1998.
1002 Roger, J. C., Mallet, M., Dubuisson, P., Cachier, H., Vermote, E., Dubovik, O.,
1003 and Despiau, S.: A synergetic approach for estimating the local direct
1004 aerosol forcing: applications to an urban zone during the ESCOMPTE
1005 experiment, J. Geophys. Res., 111, D13208,
1006 https://doi.org/10.1029/2005JD006361, 2006.
1007 Russell, P. B., Bergstrom, R. W., Shinozuka, Y., Clarke, A. D., DeCarlo, P. F.,
1008 Jimenez, J. L., Livingston, J. M., Redemann, J., Dubovik, O., and Strawa,
1009 A.: Absorption Angstrom Exponent in AERONET and related data as an
1010 indicator of aerosol composition, Atmos. Chem. Phys., 10, 1155–1169,
1011 https://doi.org/10.5194/acp-10-1155-2010, 2010.
1012 Shen, L., Zhao, C., Ma, Z., Li, Z., Li, J., and Wang, K.: Observed decrease of

summer sea-land breeze in Shanghai from 1994 to 2014 and its association with urbanization, Atmos. Res., doi:10.1016/j.atmosres.2019.05.007, 2019.

Shettle, E. P., and Fenn, R. W.: Models for the aerosols of the lower atmosphere and the effects of humidity variations on their optical properties. AFCRL Tech. Rep. 79 0214, Air Force Cambridge Research Laboratory, Hanscom Air Force Base, MA, 100 pp, 1979.

Stamnes, K., Tsay, S. C., Wiscombe, W., and Jayaweera, K.: Numerically stable algorithm for discrete-ordinate-method radiative transfer in multiple scattering and emitting layered media, Appl. Optics., 27, 2502–2509, https://doi.org/10.1364/ao.27.002502, 1988.

Su, X. L., Wang, Q., Li, Z. Q., Calvello, M., Esposito, F., Pavese, G., Lin, M. J., Cao, J. J., Zhou, C. Y., Li, D. H., Xu, H.: Regional transport of anthropogenic pollution and dust aerosols in spring to Tianjin — A coastal megacity in China, Sci. Total Environ., 584-585, 381-392, https://doi.org/10.1016/j.scitotenv.2017.01.016, 2017.

Sun, J. Y., Zhang, Q., Canagaratna, M. R., Zhang, Y. M., Ng, N. L., Sun, Y. L., Jayne, J. T., Zhang, X. C., Zhang, X. Y., and Worsnop, D. R.: Highly time- and size-resolved characterization of submicron aerosol particles in Beijing using an Aerodyne Aerosol Mass Spectrometer, Atmos. Environ., 44, 131–140, 2010.

Sun, T., Che, H., Qi, B., Wang, Y., Dong, Y., Xia, X., Wang, H., Gui, K., Zheng, Y., Zhao, H., Ma, Q., Du, R., and Zhang, X.: Aerosol optical characteristics and their vertical distributions under enhanced haze pollution events: effect of the regional transport of different aerosol types over eastern China, Atmos. Chem. Phys., 18, 2949–2971, https://doi.org/10.5194/acp-18-2949-2018, 2018.

Takamura, T., and Nakajima, T.: Overview of SKYNET and its activities, Opt. Pura Apl., 37, 3303–3308, 2004.

Tao, R., Che, H. Z., Chen, Q. L., Wang, Y. Q., Sun, J. Y., Zhang, X. C., Lu, S.,

Guo, J. P., Wang, H., and Zhang, X.Y.: Development of an integrating sphere calibration method for Cimel sunphotometers in China aerosol remote sensing network, Particuology 13, 88–99. https://doi.org/10.1016/j.partic.2013.04.009, 2014.

Twomey, S. A., Piepgrass, M., and Wolfe, T. L.: An assessment of the impact of pollution on the global cloud albedo, Tellus, 36B, 356–366, https://doi.org/10.1111/j.1600-0889.1984.tb00254.x, 1984.

Wan, X., Kang, S.C., Wang, Y.S., Xin, J.Y., Liu, B., Guo, Y.H., Wen, T.X., Zhang, G.S., and Cong, Z.Y.: Size distribution of carbonaceous aerosols at a high-altitude site on the central Tibetan Plateau (Nam Co Station, 4730m a.s.l.), Atmos. Res., 153, 155–164, https://doi.org/10.1016/j.atmosres.2014.08.008, 2015.

Wang, X., Huang, J.P., Ji, M.X., and Higuchi, K.: Variability of east Asia dust events and their long-term trend, Atmos. Environ., 42, 3156–3165, http://dx.doi.org/ 10.1016/j.atmosenv.2007.07.046, 2007.

Wang, L. C., Gong, W., Xia, X. A., Zhu, J., Li, J., and Zhu, Z. M.: Long-term observations of aerosol optical properties at Wuhan, an urban site in Central China, Atmos. Environ., 101, 94–102, DOI: 10.1016/j.atmosenv.2014.11.021, 2015.

Wang, P., Che, H. Z., Zhang, X. C., Song, Q. L., Wang, Y. Q., Zhang, Z. H., Dai, X., and Yu, D. J.: Aerosol optical properties of regional background atmosphere in Northeast China, Atmos. Environ., 44, 4404–4412, DOI: 10.1016/j.atmosenv.2010.07.043 , 2010.

Wang, Z., Liu, D., Wang, Y., Wang, Z., and Shi, G.: Diurnal aerosol variations do affect daily averaged radiative forcing under heavy aerosol loading observed in Hefei, China, Atmos. Meas. Tech., 8, 2901–2907, https://doi.org/10.5194/amt-8-2901-2015, 2015.

Wehrli, C.: Calibration of filter radiometers for the GAW Aerosol Optical Depth network at Jungfraujoch and Mauna Loa, in: Proceedings of ARJ Workshop, SANW Congress, Davos, Switzerland, 70–71, 2002.

1073 Whitey, K. T.: The physical characteristics of sulfur aerosols. Atmos. Environ.,
1074 41(supp-S), 25-49, DOI: 10.1016/j.atmosenv.2007.10.057, 1978.
1075 Wu, Y.F., Zhang, R.J., Pu, Y.F., Zhang, L.M., Ho, K.F., and Fu, C.B.: Aerosol
1076 optical properties observed at a semi-arid rural site in Northeastern China,
1077 Aerosol. Air. Qual. Res., 12,503–514, DOI: 10.4209/aaqr.2011.11.0202 ,
1078 2012.
1079 Xia, C., Sun, J. Y., Qi, X. F., Shen, X. J., Zhong, J. T., Zhang, X. Y., Wang, Y. Q.,
1080 Zhang, Y. M., and Hu, X. Y.: Observational study of aerosol hygroscopic
1081 growth on scattering coefficient in Beijing: A case study in March of 2018,
1082 Sci. Total Environ., 685, 239-247, 2019.
1083 Xia, X.: A closer looking at dimming and brightening in China during 1961–
1084 2005, Ann. Geophys., 28, 1121–1132, doi:10.5194/angeo-28-1121-2010,
1085 2010.
1086 Xia, X., Chen, H., Goloub, P., Zong, X., Zhang, W., and Wang, P.:
1087 Climatological aspects of aerosol opticalproperties in North China Plain
1088 based on ground and satellite remote-sensing data, J. Quant. Spectrosc.
1089 Ra., 127, 12–23, DOI: 10.1016/j.jqsrt.2013.06.024, 2013.
1090 Xie, C., Nishizawa, T., Sugimoto, N., Matsui, I., and Wang, Z.: Characteristics
1091 of aerosol optical properties in pollution and Asian dust episodes over
1092 Beijing, China. Appl. Opt., 47, 4945-4951, DOI: 10.1364/AO.47.004945,
1093 2008.
1094 Xie, S., Liu, X., Zhao, C., and Zhang, Y.: Sensitivity of CAM5-Simulated Arctic
1095 Clouds and Radiation to Ice Nucleation Parameterization, J. Climate., 26,
1096 5981-5999, doi:10.1175/jcli-d-12-00517.1, 2013.
1097 Xin, J., Wang Y, Li, Z.Q., Wang, P.C., Hao, W.M., Nordgren, B.L., Wang, S.G.,
1098 Liu, G.R., Wang, L.L., Wen, T.X., Sun, Y., and Hu, B.: Aerosol optical
1099 depth (AOD) and Ångström exponent of aerosols observed by the
1100 Chinese Sun Hazemeter Network from August 2004 to September 2005, J.
1101 Geophys. Res., 112, D05203, DOI: 10.1029/2006JD007075, 2007
1102 Xin, J.Y., Wang, L.L., Wang, Y.S., Li, Z., and Wang, P.: Trends in aerosol

optical properties over the Bohai Rim in Northeast China from 2004 to 2010, Atmos. Environ., 45, 6317–6325, DOI: 10.1016/j.atmosenv.2011.08.052, 2011.

Xin J, Wang Y, Pan Y, Ji, D., Liu, Z., Wen, T.X., Wang, Y.H., Li, X.R., Sun, Y., Sun, J., Wang, P.C., Wang, G.H., Wang, X.M., Cong, Z.Y., Song, T., Hu, B., Wang, L.L., Tang, G.Q., Gao, W.K., Guo, Y.H., Miao, H.Y., Tian, S.L., and Wang, L.: The campaign on atmospheric aerosol research network of China: CARE-China, Bulletin of the American Meteorological Society., 96, 1137-1155, https://doi.org/10.1175/BAMS-D-14-00039.1, 2015.

Yang, X., Zhao, C., Zhou, L., Li, Z., Cribb, M., and Yang, S.: Wintertime cooling and a potential connection with transported aerosols in Hong Kong during recent decades, Atmos. Res., 211, 52–61, doi:10.1016/j.atmosres.2018.04.029, 2018.

Yang, X., Zhao, C., Zhou, L., Wang, Y., and Liu, X.: Distinct impact of different types of aerosols on surface solar radiation in China, J. Geophys. Res.-Atmospheres, 121, 6459–6471. DOI: https://doi.org/10.1002/2016jd024938, 2016.

Yang, Y., Zhao, C., Dong, X., Fan, G., Zhou, Y., Wang, Y., Zhao, L., Lv, F., and Yan, F.: Toward understanding the process-level impacts of aerosols on microphysical properties of shallow cumulus cloud using aircraft observations, Atmos. Res., doi:10.1016/j.atmosres.2019.01.027, 2019.

Yang, Y., Zhao, C., Sun, L., and Wei, J.: Improved aerosol retrievals over complex regions using NPP Visible Infrared Imaging Radiometer Suite observations, Earth. Space. Sci., doi:10.1029/2019ea000574, 2019.

Yuan, Y., Shuai, Y., Li, X.W., Liu, B., and Tan, H.P.: Using a new aerosol relative optical thickness concept to identify aerosol particle species, Atmos. Res., 150, 1–11, DOI: 10.1016/j.atmosres.2014.07.007, 2014.

Zhang, L., Sun, J. Y., Shen, X. J., Zhang, Y. M., Che, H., Ma, Q. L., Zhang, Y. W., Zhang, X. Y., and Ogren, J. A.: Observations of relative humidity effects on aerosol light scattering in the Yangtze River Delta of China,

1133 Atmos. Chem. Phys., 15, 8439-8454,
1134 https://doi.org/10.5194/acp-15-8439-2015, 2015.
1135 Zhang, M., Ma, Y., Gong, W., Liu, B., Shi, Y., and Chen, Z.: Aerosol optical
1136 properties and radiative effects: Assessment of urban aerosols in central
1137 China using 10-year observations, Atmos. Environ., 182, 275-285, DOI:
1138 10.1016/j.atmosenv.2018.03.040, 2018
1139 Zhang, R., Jing, J., Tao, J., Hsu, S.-C., Wang, G., Cao, J., Lee, C.S.L., Zhu, L.,
1140 Chen, Z., Zhao, Y., and Shen, Z.: Chemical characterization and source
1141 apportionment of PM2.5 in Beijing: seasonal perspective, Atmos. Chem.
1142 Phys., 13, 7053–7074, http://dx.doi.org/10.5194/acp-13-7053-2013, 2013
1143 Zhao, C., and Garrett, T. J.: Effects of Arctic haze on surface cloud radiative
1144 forcing, Geophys. Res. Lett., 42, 557–564. doi:10.1002/2014gl062015,
1145 2015.
1146 Zhao, C., Lin, Y., Wu, F., Wang, Y., Li, Z., Rosenfeld, D., and Wang, Y.:
1147 Enlarging Rainfall Area of Tropical Cyclones by Atmospheric Aerosols,
1148 Geophys. Res. Lett., doi:10.1029/2018gl079427, 2018.
1149 Zhao, C., Wang, Y., Shi, X., Zhang, D., Wang, C., Jiang, J. H., Zhang, Q., and
1150 Fan, H.: Estimating the contribution of local primary emissions to
1151 particulate pollution using high-density station observations, J. Geophys.
1152 Res.-Atmospheres, doi:10.1029/2018jd028888, 2019.
1153 Zhao, H., Che, H., Ma, Y., Xia, X., Wang, Y., Wang, P., and Wu, X.: Temporal
1154 variability of the visibility, particulate matter mass concentration and
1155 aerosol optical properties over an urban site in Northeast China, Atmos.
1156 Res., 166, 204–212, DOI: 10.1016/j.atmosres.2015.07.003, 2015.
1157 Zhao H., Che H., Wang Y., Wang H., Ma Y., and Wang Y.: Investigation of the
1158 Optical Properties of Aerosols over the Coastal Region at Dalian,
1159 Northeast China, Atmosphere., 7(8), 103, DOI: 10.3390/atmos7080103,
1160 2016
1161 Zhao, H., Che, H., Xia, X., Wang, Y., Wang, H., Wang, P., Ma, Y., Yang, H., Liu,
1162 Y., Wang, Y., Gui, K., Sun, T., Zheng, Y., and Zhang, X.: Multi-year

ground-based measurements of aerosol optical properties and direct radiative effect over different surface types in northeastern China, J. Geophys. Res.-Atmos., 123, 13,887–13,916, https://doi.org/10.1029/2018JD029141, 2018

Zhang, K., Zhao, C., Fan, H., Yang, Y., and Sun, Y.: Toward Understanding the Differences of PM2.5 Characteristics Among Five China Urban Cities, Asia-Pac. J. Atmos. Sci., doi:10.1007/s13143-019-00125-w, 2019.

Zheng, C., Zhao, C., Zhu, Y., Wang, Y., Shi, X., Wu, X., Chen, T.,Wu, F., and Qiu, Y.: Analysis of influential factors for the relationship between PM2.5 and AOD in Beijing, Atmos. Chem. Phys., 17, 13473–13489, doi: 10.5194/acp-17-13473-2017, 2017.

Zheng, Y., Che, H., Xia, X., Wang, Y., Wang, H., Wu, Y., Tao, J., Zhao, H., An, L., Li, L., Gui, K., Sun, T., Li, X., Sheng, Z., Liu, C., Yang, X., Liang, Y., Zhang, L., Kuang, X., Luo, S., and You, Y.: Five-year observation of aerosol optical properties and its radiative effects to planetary boundary layer during air pollution episodes in North China: Intercomparison of a plain site and a mountainous site in Beijing, Sci. Total. Environ., 674, 140-158, 2019.

Zhu, J., Che, H., Xia, X., Chen, H. B., Goloub, P., and Zhang, W.: Column-integrated aerosol optical and physical properties at a regional background atmosphere in North China Plain, Atmos. Environ., 84, 54–64, DOI: 10.1016/j.atmosenv.2013.11.019, 2014.

Zhuang, B., Wang, T., Li, S., Liu, J., Talbot, R., Mao, H., Yang, X., Fu, C., Yin, C., Zhu, J., Che, H., and Zhang, X.: Optical properties and radiative forcing of urban aerosols in Nanjing over China, Atmos. Environ., 83, 43–52, DOI: 10.1016/j.atmosenv.2013.10.052, 2014.

Figure captions

Figure 1. Annual spatial distribution of aerosol volume-size distributions at the CARSNET sites

Figure 2. Annual spatial distribution of aerosol optical depth (AOD) at 440 nm at the CARSNET sites

Figure 3. Annual spatial distribution of extinction Ångström exponent (AE) 440-870 nm at the CARSNET sites

Figure 4. Annual spatial distribution of fine mode fraction at the CARSNET sites

Figure 5. Annual spatial distribution of the single scattering albedo (SSA) at 440 nm at the CARSNET sites

Figure 6. Annual spatial distribution of absorption aerosol optical depth (AAOD) at 440 nm at the CARSNET sites

Figure 7. Annual spatial distribution of direct aerosol radiative effect at the bottom of the atmosphere at the CARSNET sites

Figure 8. Annual spatial distribution of direct aerosol radiative effect at the top of the atmosphere at the CARSNET sites

Figure 9. Annual spatial distribution of the aerosol type classification of types I–VII at the CARSNET sites

Table 1 The aerosol type classification based on the optical properties

Figure 1. Annual spatial distribution of aerosol volume-size distributions at the CARSNET sites

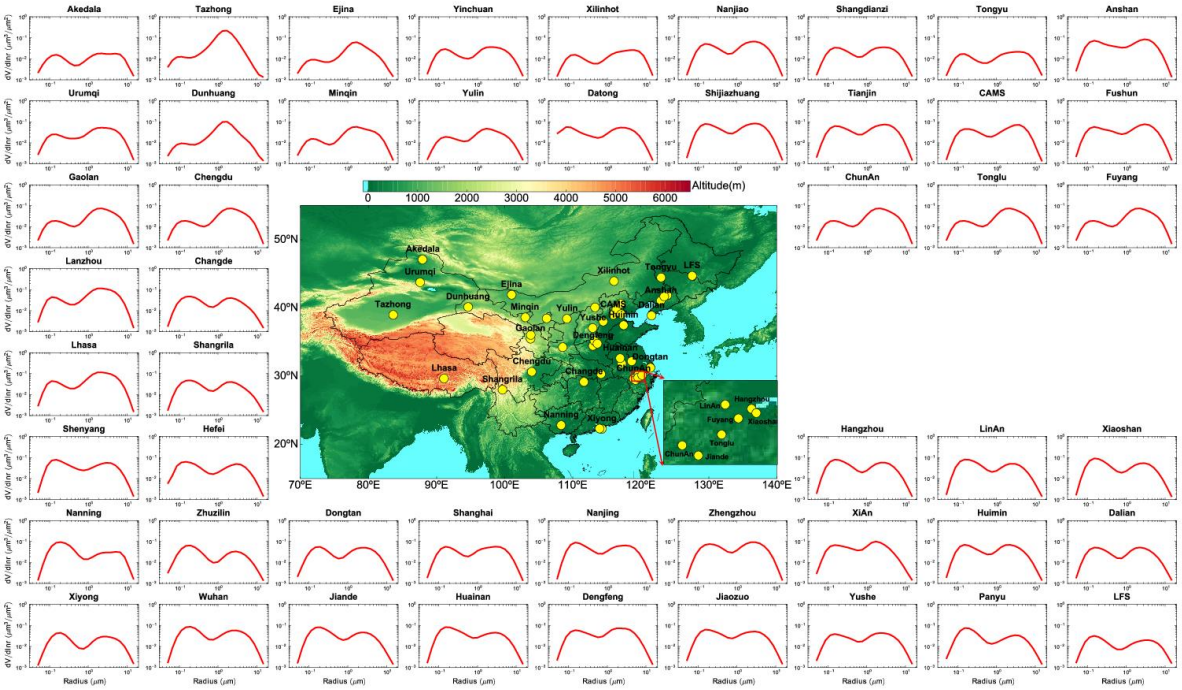

Figure 2. Annual spatial distribution of aerosol optical depth (AOD) at 440 nm at the CARSNET sites

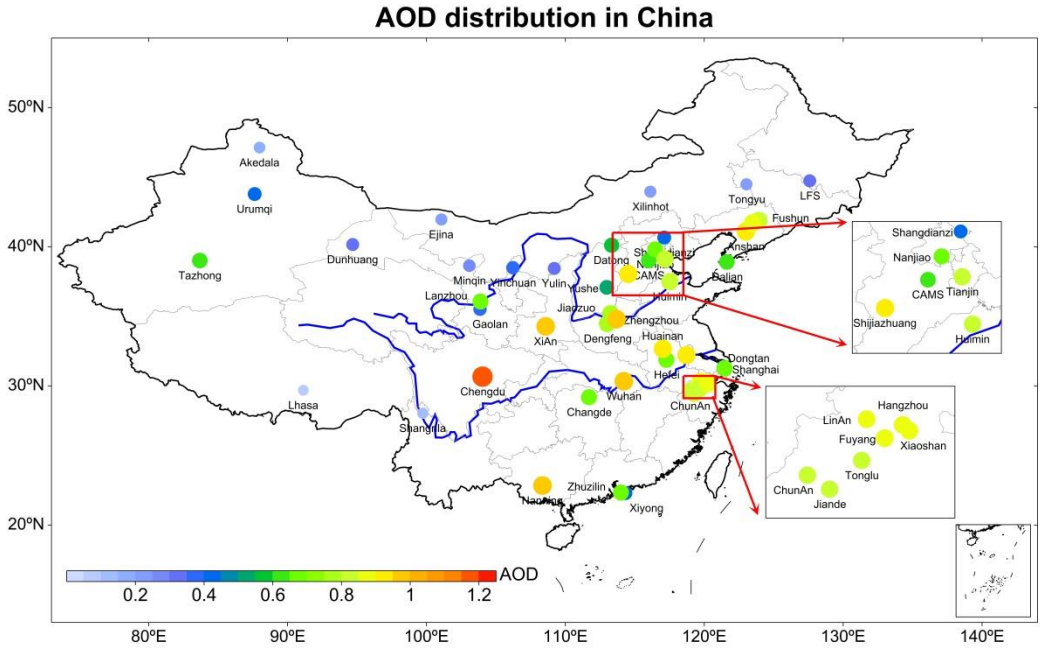

Figure 3. Annual spatial distribution of extinction Ångström exponent (AE) 440-870 nm at the CARSNET sites

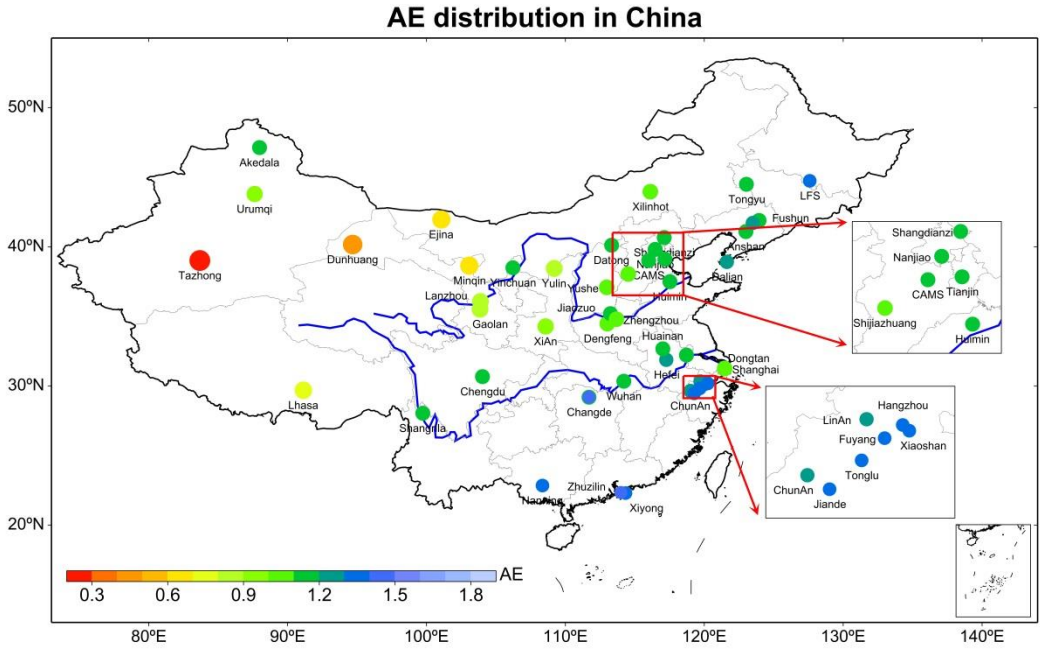

Figure 4. Annual spatial distribution of fine mode fraction at the CARSNET sites

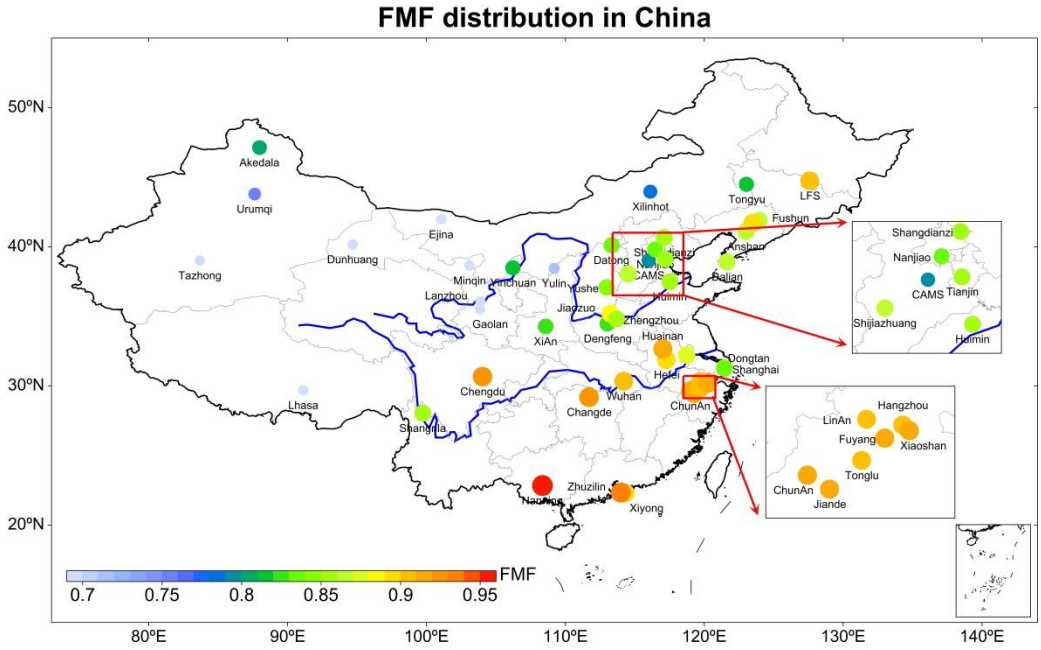

Figure 5. Annual spatial distribution of the single scattering albedo (SSA) at 440 nm at the CARSNET sites

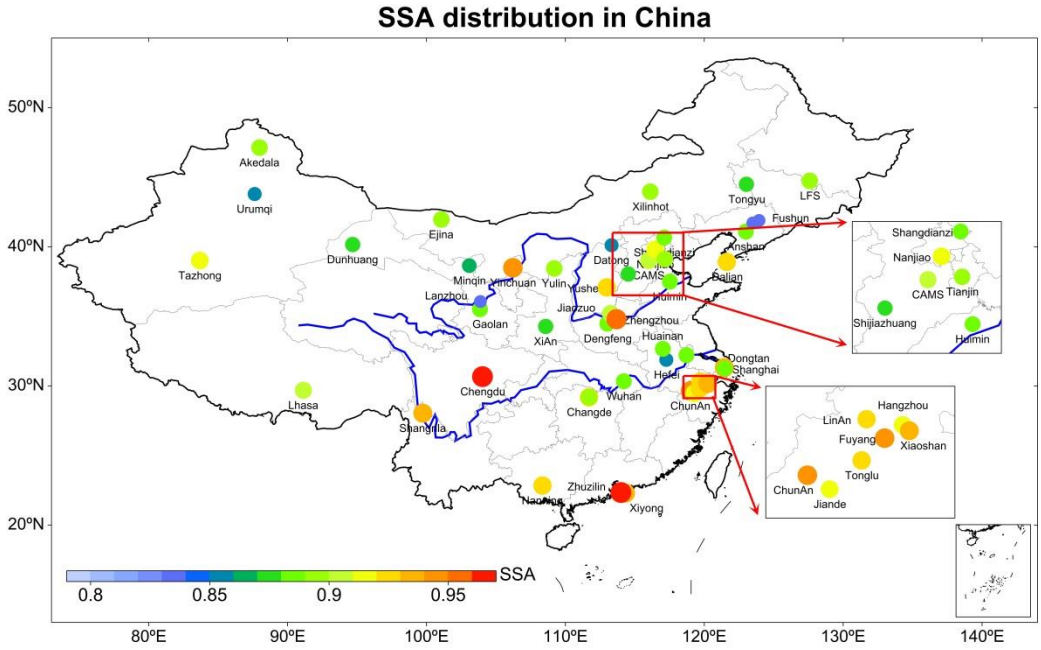

Figure 6. Annual spatial distribution of absorption aerosol optical depth (AAOD) at 440 nm at the CARSNET sites

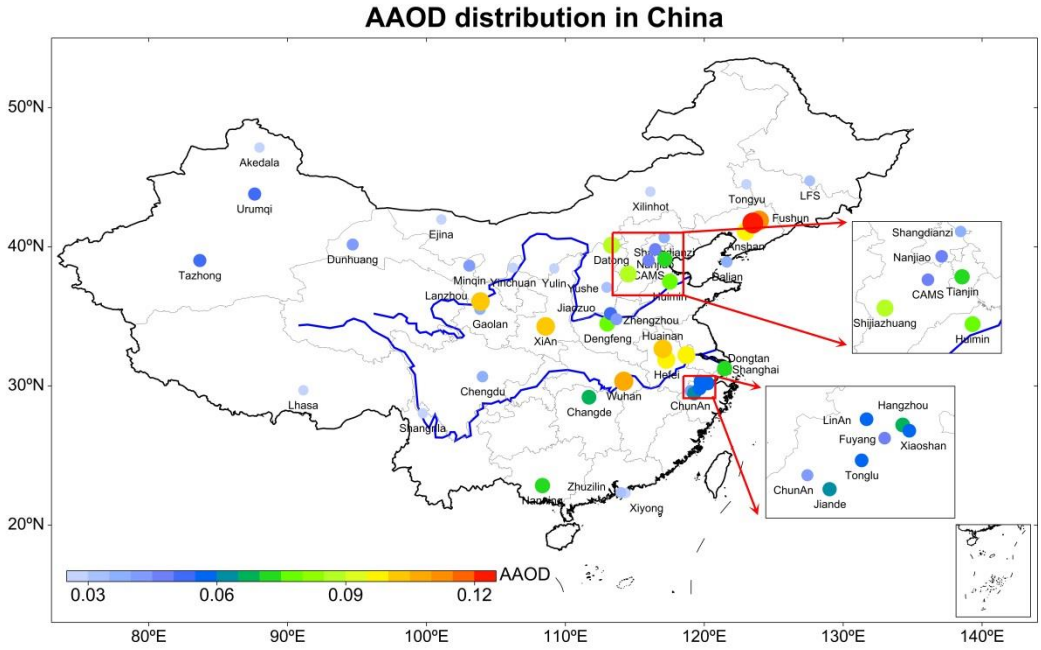

Figure 7. Annual spatial distribution of direct aerosol radiative effect at the bottom of the atmosphere at the CARSNET sites

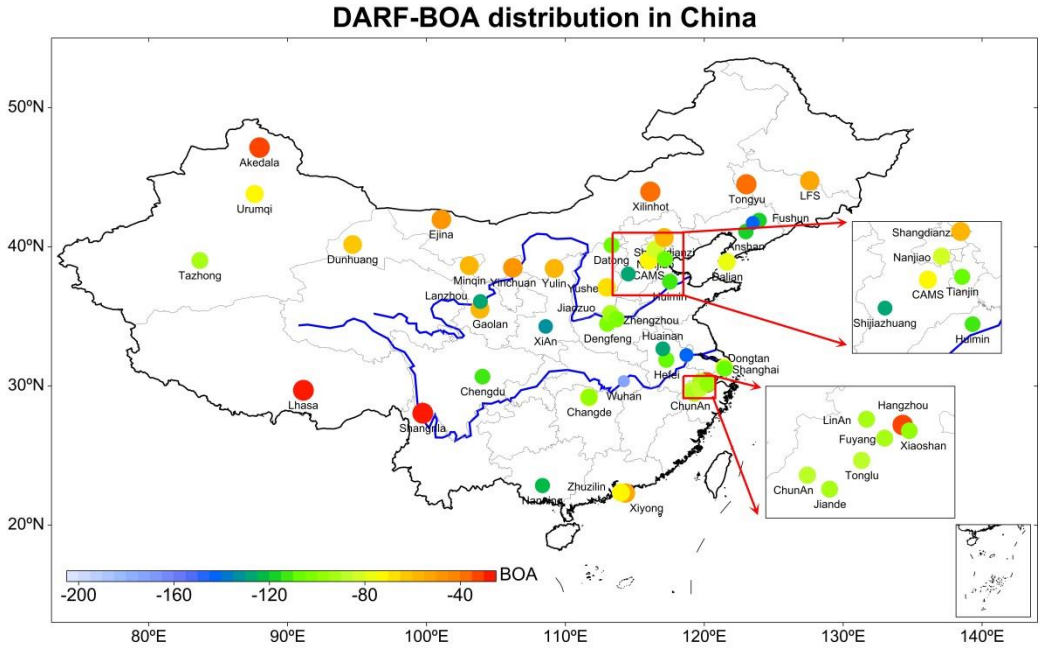

Figure 8. Annual spatial distribution of direct aerosol radiative effect at the top of the atmosphere at the CARSNET sites

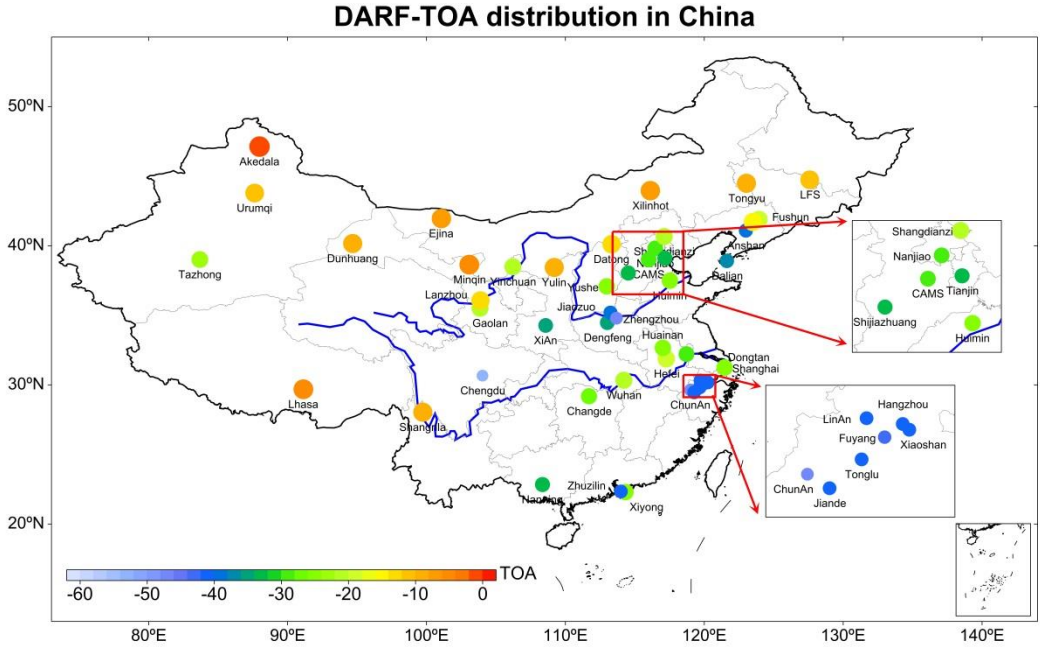

Figure 9. Annual spatial distribution of the aerosol type classification of types I–VII at the CARSNET sites

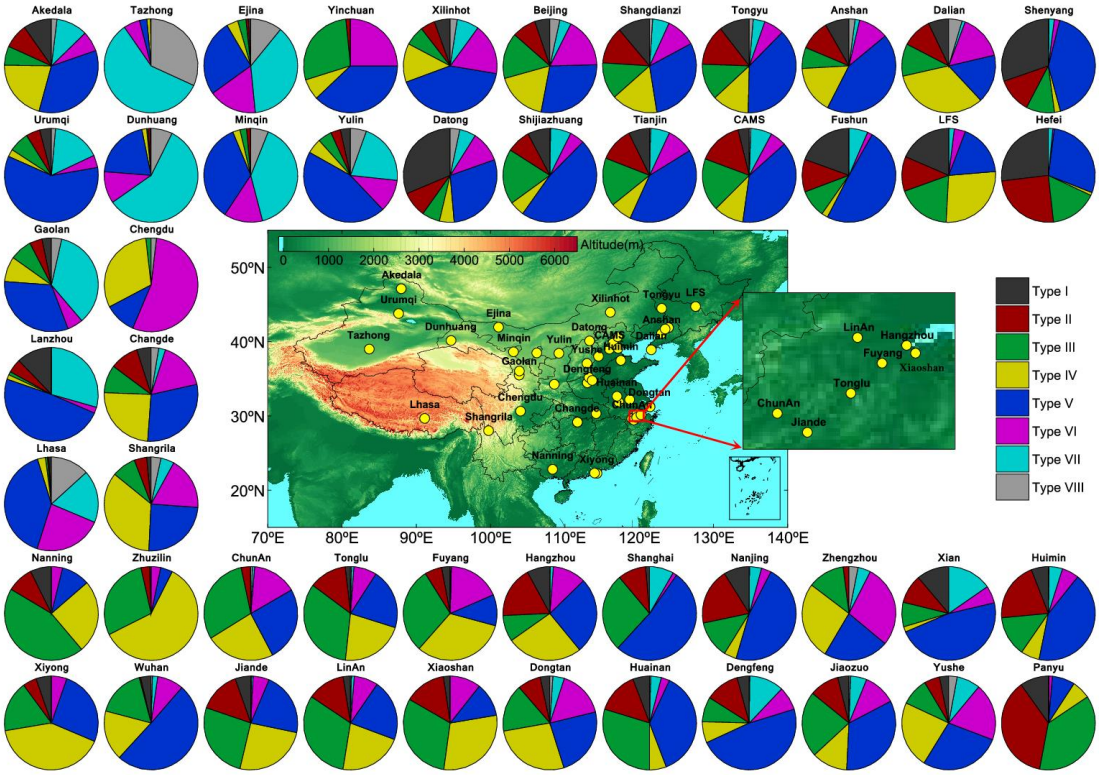

Table 1. The aerosol type classification based on the optical properties.

Type	EAE	SSA	absorbing properties and particle size
I	EAE > 1.20	$SSA_{440nm} \leqslant 0.85$	fine-mode particles with highly-absorbing
II	EAE > 1.20	$0.85 \leqslant SSA_{440nm} < 0.90$	fine-mode particles with moderately-absorbing
III	EAE > 1.20	$0.90 \leq SSA_{440nm} < 0.95$	fine-mode particles with slightly-absorbing
IV	EAE > 1.20	$SSA_{440nm} > 0.95$	fine-mode particles with weakly-absorbing
V	$0.60 \leq EAE < 1.20$	$SSA_{440nm} \leq 0.95$	mixed-absorbing particles
VI	$0.60 \leq EAE < 1.20$	$SSA_{440nm} > 0.95$	mixed-slightly absorbing particles
VII	$EAE \leq 0.60$	$SSA_{440nm} \leq 0.95$	coarse mode particles with strongly absorbing (mainly dust)
VIII	$AE \leq 0.60$	$SSA_{440nm} > 0.95$	coarse-mode particles with weakly-absorbing

Appendix

Table 1. Site information for the 50 CARSNET sites used in this study

No.	Site Name	Long.	Lat.	Alt.	Site information	Obs. Num	Period
					Remote sites (three sites)		
1	Akedala	47.12	87.97	562.0	55 km west of Fuhai county, Xinjiang province, and 250–300 km southeast of Kazakestan.	947	2010-2017
2	Lhasa	29.67	91.13	3663.0	In the center of Lhasa city, Qinghai-Xizang Plateau.	437	2012-2017
3	Shangri-La	28.02	99.73	3583.0	12 km northeast of Shangri-La county, Diqing area, Yunnan province	325	2013-2017
					Arid and semi-arid sites (six sites)		
4	Dunhuang	40.15	94.68	1139.0	1.5 km northeast of Dunhuang city, Gansu province; near Kumutage Desert of China	2030	2012-2017
5	Ejina	41.95	101.07	940.5	West ofIner-Mongolia Province, near Mongolia and Badanjilin desert	1970	2013-2017
6	Minqin	38.63	103.08	1367.0	In Minqin county, east to Tenggeli desert and north to Badanjilin Desert, Gansu Province	481	2013-2017
7	Tazhong	39.00	83.67	1099.4	In the middle of Takilamakan Desert, Xinjiang Province	1279	2013-2017
8	Xilinhot	43.95	116.12	1003.0	5 km southeast of Xilinhot City, near Hunshandake sand-land, Inner-Mongolia Province,	1464	2013-2017
9	Tongyu	44.42	122.87	151.0	In Tonyu city, west of Jilin Province	817	2010-2011
					Rural sites on the Chinese Loess Plateau or nearby (three sites)		
10	Mt.Gaolan	36.00	103.85	2161.6	5 km north of Lanzhou city in Gansu province	769	2015-2016
11	Yulin	38.43	109.20	1135.0	10 km north of Yulin city in Shaanxi province	716	2010-2016
12	Datong	40.10	113.33	1067.3	9 km of Datong City, but within area of rapid urbanization, Shanxi Province	914	2014-2017
					Rural sites in eastern China (15 sites)		
13	Changde	29.17	111.70	565.0	18 km northwest from Changde city, Hunan province.	344	2013-2016
14	Dongtan	31.52	121.96	10.0	In the Chongmin Island, 30km east of Shanghai city	986	2012-2016
15	ChunAn	29.61	119.05	171.4	151 km southwest from Hangzhou city, Zhejiang province.	1286	2011-2015
16	Huimin	37.48	117.53	11.7	100 km Northeast of Jinan City, Shandong Province	2243	2009-2017
17	Lin'an	30.30	119.73	138.6	150 km northeast of Shanghai, and 50 km west of Hangzhou city, Zhejiang province	1834	2011-2015
18	Mt.Longfeng	44.73	127.60	330.5	In Wuchang county, 175 km northeast of Harbin city, Heilongjiang Province	1515	2012-2016
19	Fuyang	30.07	119.95	17.0	44.1 km southwest from Hangzhou city, Zhejiang province.	710	2014-2015
20	Shangdianzi	40.65	117.12	293.0	In Miyun county, 150 km northeast to Beijing city.	1520	2014-2017
21	Yushe	37.07	112.98	1041.5	1.5 km east of Yushe city in Shanxi Province	1479	2013-2017
22	Dengfeng	34.46	113.02	350.0	75 km Southwest of Zhengzhou City, Henan Province	712	2013
23	Huainan	32.65	117.02	52.0	In the central of Hefei City, Anhui Province	794	2014-2015
24	Jiande	29.45	119.28	89.0	In the southwest from Hangzhou city, Zhejiang province.	1550	2011-2015
25	Tonglu	29.80	119.64	46.1	100 km northwest from Hangzhou city, Zhejiang province.	1717	2011-2015
26	Xiaoshan	30.16	120.25	14.0	In the south of Hangzhou city, Zhejiang province.	600	2014-2015
27	Xiyong	22.28	114.33	155.2	In the eastern of Shenzhen city, Guangdong province.	189	2016
					Urban sites (23 sites)		
28	Anshan	41.08	123.00	23.0	In Anshan city, central Liaoning province	193	2009-2013
29	Beijing-Nanjiao	39.80	116.47	31.3	In the southeast Beijing at city margin	1732	2014-2017
30	Beijing-CAMS	39.93	116.32	106.0	Chinese Academy of Meteorological Sciences in Beijing	1113	2012-2018
31	Chengdu	30.65	104.03	496.0	In Chengdu city, Sichuan province.	55	2014-2015
32	Dalian	38.90	121.63	91.5	Southeast coastal city in Liaoning Province	736	2012-2015
33	Fushun	41.88	123.95	80.0	In Fushun city, central Liaoning province.	231	2009-2013
34	Hangzhou	30.23	120.17	42.0	In Hangzhou city, Zhengjiang province.	1663	2011-2015

35	Hefei	31.98	116.38	92.0	In Hefei city, Anhui province.	197	2016
36	Jiaozuo	35.18	113.25	113.0	In the center of Jiaozuo city, Henan province.	981	2016-2017
37	Lanzhou	36.05	103.88	1517.3	In Lanzhou city, Gansu province.	1493	2013-2017
38	Nanjing	32.05	118.77	99.3	In Nanjing city, Jiangsu province	1258	2007-2015
39	Nanning	22.82	108.35	172.0	In Nanning city, Guangxi province	286	2013-2017
40	Panyu	23	113.35	145.0	In district of Guangzhou city, Guangdong Province	436	2012-2016
41	Shanghai	31.22	121.55	14.0	In Pudong district of Shanghai city	144	2016
42	Shenyang	41.77	123.50	60.0	In Shenyang city, central Liaoning province.	541	2009-2013
43	Tianjin	39.10	117.17	3.3	Northern coastal city in North China Plain	1705	2013-2017
44	Urumqi	43.78	87.62	935.0	In Urumuqi city, Xijiang province	1411	2012-2017
45	Xi'an	34.43	108.97	363.0	20 km north of center of Xian city, but within Jing RiverIndustrial District, Shaanxi province	652	2012-2016
46	Yinchuan	38.48	106.22	1111.5	In Yinchuan city, Ningxia province.	124	2017
47	Zhengzhou	34.78	113.68	99.0	In Zhengzhou city, Henan province.	1485	2013-2017
48	Shijiazhuang	38.03	114.53	75.0	In the center of Shijiazhuang city, Hebei province.	1178	2015-2017
49	Wuhan	30.32	114.21	30	In the center of Wuhan city, Hubei province	220	2008
50	Zhuzilin	22.32	114.00	63.0	In the central of Shenzhen city, Guangdong province.	915	2010-2017

1306 **Table 2. Annual data for aerosol microphysical properties, optical and direct radiative parameters**

No.	Site	[a]ReffT	[a]ReffF	[a]ReffC	[a]VolT	[a]VolF	[a]VolC	[a]AODt	[b]Alpha	[a]FMF	[a]SSAT	[a]Image	[a]Real	[a]AAOD	[a]BOA	[a]TOA
Remote sites (3 sites)																
1	Akedala	0.36	0.14	2.45	0.06	0.02	0.04	0.17	1.13	0.81	0.90	0.0117	1.4540	0.02	-33.65	-0.42
2	Lhasa	0.64	0.13	2.26	0.05	0.01	0.04	0.10	0.77	0.66	0.90	0.0106	1.5541	0.01	-22.13	-5.04
3	Shangri-La	0.39	0.14	2.33	0.03	0.01	0.02	0.10	1.19	0.85	0.93	0.0086	1.4626	0.01	-17.43	-8.93
	Average	0.47	0.14	2.35	0.05	0.01	0.03	0.12	1.03	0.77	0.91	0.0103	1.4902	0.01	-24.40	-4.79
Arid and semi-arid sites (6 sites)																
4	Dunhuang	0.62	0.14	1.52	0.15	0.02	0.13	0.33	0.48	0.44	0.88	0.0103	1.5491	0.04	-63.61	-8.96
5	Ejina	0.56	0.14	1.78	0.11	0.02	0.09	0.24	0.64	0.52	0.89	0.0116	1.5265	0.03	-47.66	-7.20
6	Minqin	0.56	0.13	1.87	0.13	0.02	0.11	0.30	0.68	0.59	0.86	0.0145	1.5430	0.04	-59.83	-5.01
7	Tazhong	0.71	0.14	1.38	0.30	0.03	0.27	0.60	0.25	0.35	0.92	0.0054	1.5257	0.05	-91.20	-23.49
8	Xilinhot	0.48	0.13	2.45	0.08	0.02	0.05	0.21	1.03	0.78	0.89	0.0139	1.5183	0.02	-37.14	-7.47
9	Tongyu	0.39	0.13	2.36	0.07	0.02	0.05	0.23	1.16	0.82	0.88	0.0179	1.5377	0.03	-39.13	-8.87
	Average	0.55	0.14	1.89	0.14	0.02	0.12	0.32	0.71	0.58	0.89	0.0123	1.5334	0.03	-56.43	-10.17
Rural sites on the Chinese Loess Plateau or nearby (3 sites)																
10	Mt.Gaolan	0.58	0.14	2.03	0.16	0.03	0.13	0.36	0.81	0.64	0.89	0.0108	1.5154	0.04	-59.36	-20.87
11	Yulin	0.53	0.15	2.05	0.11	0.03	0.08	0.32	0.84	0.72	0.89	0.0122	1.5070	0.03	-56.81	-9.09
12	Datong	0.35	0.13	2.15	0.19	0.09	0.10	0.58	1.15	0.83	0.86	0.0171	1.4905	0.09	-107.86	-13.71
	Average	0.49	0.14	2.08	0.15	0.05	0.10	0.42	0.93	0.73	0.88	0.0134	1.5043	0.05	-74.67	-14.56
Rural sites in eastern China (15 sites)																
13	Changde	0.32	0.16	2.18	0.14	0.07	0.07	0.58	1.15	0.88	0.93	0.0101	1.4619	0.04	-75.33	-31.44
14	Dongtan	0.37	0.16	2.12	0.17	0.08	0.09	0.62	1.21	0.86	0.93	0.0080	1.4624	0.04	-79.41	-33.18
15	ChunAn	0.30	0.18	2.30	0.19	0.12	0.08	0.81	1.22	0.92	0.94	0.0066	1.4095	0.04	-86.49	-46.48
16	Huimin	0.36	0.15	2.07	0.22	0.10	0.12	0.83	1.14	0.86	0.89	0.0147	1.4852	0.08	-111.58	-25.49

17	Lin'an	0.29	0.17	2.24	0.21	0.12	0.09	0.87	1.29	0.91	0.93	0.0089	1.4172	0.06	-93.09	-41.73
18	Mt.Longfeng	0.28	0.15	2.44	0.08	0.04	0.04	0.34	1.38	0.90	0.89	0.0165	1.4647	0.03	-51.17	-11.34
19	Fuyang	0.29	0.17	2.28	0.21	0.13	0.09	0.89	1.31	0.92	0.94	0.0070	1.4147	0.05	-91.69	-42.29
20	Shangdianzi	0.40	0.15	2.33	0.12	0.05	0.07	0.43	1.17	0.86	0.89	0.0148	1.4840	0.04	-59.99	-20.58
21	Yushe	0.41	0.15	2.18	0.14	0.06	0.08	0.50	1.07	0.84	0.92	0.0090	1.4878	0.03	-66.72	-25.99
22	Dengfeng	0.39	0.15	2.03	0.23	0.09	0.13	0.79	1.02	0.83	0.89	0.0131	1.4782	0.08	-104.78	-35.84
23	Huainan	0.30	0.17	2.25	0.21	0.13	0.08	0.91	1.17	0.92	0.88	0.0166	1.4308	0.10	-129.17	-24.44
24	Jiande	0.29	0.17	2.18	0.20	0.12	0.08	0.84	1.34	0.91	0.92	0.0099	1.4085	0.06	-91.06	-40.07
25	Tonglu	0.29	0.17	2.20	0.20	0.12	0.08	0.83	1.31	0.91	0.93	0.0091	1.4269	0.06	-89.82	-41.28
26	Xiaoshan	0.28	0.17	2.24	0.22	0.13	0.09	0.87	1.35	0.91	0.93	0.0082	1.4134	0.06	-95.23	-40.39
27	Xiyong	0.33	0.16	2.43	0.11	0.06	0.05	0.41	1.32	0.89	0.94	0.0074	1.4072	0.02	-53.18	-25.45
	Average	0.33	0.16	2.23	0.18	0.09	0.08	0.70	1.23	0.89	0.92	0.0107	1.4435	0.05	-85.25	-32.40
								Urban sites (23 sites)								
28	Anshan	0.36	0.17	2.24	0.26	0.12	0.14	0.94	1.12	0.86	0.89	0.0158	1.4759	0.10	-117.99	-39.66
29	Beijing-Nanjiao	0.45	0.15	2.33	0.19	0.07	0.12	0.65	1.12	0.84	0.92	0.0100	1.4939	0.05	-82.06	-29.43
30	Beijing-CAMS	0.50	0.16	2.37	0.19	0.07	0.12	0.65	1.12	0.79	0.90	0.0115	1.5108	0.05	-72.66	-29.10
31	Chengdu	0.34	0.21	2.26	0.26	0.16	0.10	1.17	1.12	0.92	0.97	0.0033	1.4116	0.04	-110.42	-52.21
32	Dalian	0.35	0.16	2.24	0.16	0.08	0.09	0.62	1.22	0.87	0.93	0.0095	1.4584	0.04	-75.50	-37.42
33	Fushun	0.38	0.17	2.34	0.22	0.09	0.12	0.80	1.12	0.87	0.84	0.0244	1.4954	0.11	-116.91	-19.59
34	Hangzhou	0.30	0.17	2.21	0.22	0.12	0.10	0.87	1.30	0.90	0.91	0.0109	1.4337	0.07	-31.57	-40.16
35	Hefei	0.29	0.15	2.37	0.18	0.10	0.08	0.69	1.28	0.90	0.85	0.0195	1.4253	0.10	-105.83	-19.22
36	Jiaozuo	0.35	0.16	2.17	0.20	0.10	0.10	0.76	1.14	0.88	0.91	0.0105	1.4722	0.05	-92.29	-39.35
37	Lanzhou	0.54	0.14	2.04	0.28	0.06	0.22	0.66	0.81	0.66	0.83	0.0197	1.5193	0.10	-126.17	-13.81
38	Nanjing	0.33	0.16	2.16	0.25	0.12	0.12	0.94	1.13	0.88	0.88	0.0154	1.4446	0.10	-143.38	-28.29
39	Nanning	0.30	0.18	2.53	0.20	0.13	0.06	0.97	1.36	0.95	0.92	0.0107	1.4272	0.07	-121.92	-33.35
40	Panyu	0.26	0.16	2.29	0.16	0.10	0.06	0.69	1.43	0.93	0.90	0.0137	1.4155	0.07	-96.03	-26.56

41	Shanghai	0.40	0.15	1.93	0.19	0.08	0.11	0.68	1.10	0.84	0.88	0.0142	1.4814	0.07	-106.89	-24.34
42	Shenyang	0.31	0.16	2.23	0.22	0.12	0.10	0.89	1.20	0.90	0.84	0.0253	1.4589	0.14	-144.88	-15.02
43	Tianjin	0.42	0.16	2.26	0.23	0.10	0.13	0.83	1.11	0.86	0.89	0.0134	1.4957	0.07	-108.09	-33.26
44	Urumqi	0.48	0.14	2.14	0.15	0.04	0.10	0.42	0.93	0.75	0.85	0.0192	1.5371	0.05	-70.55	-11.74
45	Xi'an	0.37	0.16	1.85	0.26	0.11	0.15	0.98	0.98	0.82	0.88	0.0150	1.4888	0.10	-132.55	-35.93
46	Yinchuan	0.38	0.14	2.02	0.11	0.04	0.07	0.37	1.12	0.81	0.94	0.0054	1.4930	0.02	-48.67	-21.89
47	Zhengzhou	0.43	0.18	2.22	0.28	0.12	0.16	0.99	1.10	0.86	0.95	0.0045	1.4626	0.04	-101.10	-46.18
48	Shijiazhuang	0.40	0.16	2.28	0.26	0.12	0.14	0.95	1.09	0.87	0.88	0.0154	1.4754	0.09	-125.05	-33.66
49	Wuhan	0.34	0.17	2.22	0.22	0.12	0.10	1.00	1.16	0.91	0.88	0.0196	1.4779	0.11	-171.80	-20.40
50	Zhuzilin	0.27	0.17	2.45	0.15	0.09	0.05	0.66	1.45	0.94	0.96	0.0049	1.4438	0.03	-73.16	-40.65
	Average	0.37	0.16	2.22	0.21	0.10	0.11	0.79	1.15	0.86	0.90	0.0136	1.4695	0.07	-103.28	-30.05

Table 1 (Continued)

[a] Optical parameters at a wavelength of 440 nm.

[b] Angström exponents between 440 and 870 nm.